BATHYMETRIC EFFECTS ON MARINE HYDROKINETIC

ARRAY PERFORMANCE

by

Garrett William Peebles

A thesis submitted in partial fulfillment
of the requirements for the degree

of

Master of Science

in

Mechanical Engineering

MONTANA STATE UNIVERSITY
Bozeman, Montana

May, 2015

ACKNOWLEDGEMENTS

I would like to thank all of the people who helped me along the way. I would have not been able to get this far without all the help and support. In particular I would like to thank Dr. Erick Johnson for the opportunity to do research on a fun and interesting topic. Dr. Johnson was the best advisor and mentor that any graduate student could hope to work for. Thank you Aunt Anitra and Uncle Jack for your continued support and encouragement on pursuing higher education. Thank you Dr. Cairns for opening up my eyes to possibility of attending graduate school and for all of your advisements during my time at Montana State. Thank you Dr. Edens for taking the time to be a part of my committee. Thanks to the Mechanical Engineering department and faculty at MSU for being the most awesome people on campus. Thank you to all of the members of the Mechanical Engineering Fluids and Computations Laboratory for their insights and collaborations. Last of all I would like to thank my parents for always being there for me.

TABLE OF CONTENTS

TABLE OF CONTENTS - CONTINUED

LIST OF FIGURES

LIST OF FIGURES CONTINUED

Figure Page

LIST OF FIGURES – CONTINUED

Figure Page

ABSTRACT

Approximately 16% of the globally generated electricity comes from conventional hydropower installations. Recent technological improvements in marine hydrokinetics (MHK), and a global demand for increased renewable energy, are enabling this technology to become a major contributor in the global energy market. MHK devices convert the kinetic energy, or energy of motion, from waves or water currents into electricity that is then transferred to the electrical grid. Wave energy converters (WECs) capitalize on the oscillatory motion of ocean waves, while current energy converters (CECs) use river, tidal, or ocean currents to generate electricity and often resemble wind turbines. Unlike wind, water currents are less intermittent, and, in the case of tidal currents, highly predictable. At present scales, individual CEC and WEC devices alone are not powerful enough to make hydrokinetic power economically feasible. Therefore, deployment of arrays of marine hydrokinetic devices is the most cost-effective method for these devices to become a major contributor in the energy market. In addition to device design and operational conditions, how these devices are deployed within a site determines their potential for power generation. The power generated depends upon inter-device proximity, where it is generally assumed more electricity is generated as the spacing between each device increases. However, most array performance studies of current-energy converters do not consider bed topography and are either inside smooth walled channels or deep, open waters. The research presented here explores the impact of site bathymetry on array performance since each deployment location is likely to have a significant impact on the optimality of an array layout. It is first shown that without boundary constraints the performance of an array does improve as the inter-device spacing is increased. Uniquely though, the normalized power and loading on an array is not transferable from an unconstrained domain to simple, sloping beds. The effects of this demonstrate the need to consider the topography of real world locations for general array designs.

INTRODUCTION

The United States, among other countries, is looking to meet future energy needs without heavy reliance on fossil fuels. Renewable energy is an attractive solution as the energy sources are not depletable and generally do not produce hazardous byproducts. Solar, wind, and water power are the most recognized renewable energy solutions. Marine hydrokinetic is a new look at an ancient form of water power that uses the kinetic energy from currents and waves to generate power. Most of the U.S. population lives along coastlines and rivers; which makes water renewable very attractive, as it readily available to areas that consume vast amounts of energy. The U.S. Department of Energy completed a resource assessment and characterization for potential energy production from marine hydrokinetic (MHK) devices. The total recoverable energy in the U.S. from current and wave MHK energy is projected to be approximately 1,700 TWh year^{-1}. This is enough energy to power around one third of the annual electrical consumption in the U.S. The recoverable energy in the continental U.S. from riverine environments is approximately 120 TWh year^{-1}. To put this in perspective 1 TWh year^{-1} is enough power to supply 85,000 U.S. households with energy for one year. Due to the enormous amount of available energy, entrepreneurial companies and the U.S. Department of Energy have been aggressively pursuing research in all aspects of marine hydrokinetics.

Marine Hydrokinetics

Marine hydrokinetics (MHK) is a modern form of water renewable. Instead of utilizing potential energy like conventional hydropower, marine hydrokinetics use kinetic energy, or the energy of motion. Marine hydrokinetics actually operate in a very similar manner to wind power, particularly for current-energy-converters. There are two main applications of marine hydrokinetics: wave and current. In wave environments the kinetic energy from ocean waves is converted to electrical energy by wave-energy-converters (WEC). Marine current hydrokinetics uses currents from the ocean or rivers to drive current-energy-converters (CEC) to generate electricity. These types of devices alone cannot produce enough energy, unless sufficiently large, to become economically feasible. To become economically viable WECs and CECs must be deployed in arrays. Arrays are a set of multiple devices within a predetermined footprint. These arrays must have many devices to be economical viable. However, arrays introduce design optimization problems based on device location within the allotted footprint. There have been multiple studies on array performance for wind turbines; which are very similar to current-energy-converters (Archer et. al. 2013, Stevens & Meneveau 2015). In these studies the wind turbines were at the same height, but the device spacing in the longitudinal and lateral directions was manipulated in an attempt to find optimal device spacing for the maximum performance. Similar studies have been performed for MHK devices (Yang et al. 2013, Archer et al. 2013). The problem for marine hydrokinetics is that the bathymetry of the systems has the potential to effect array performance. The research presented in this thesis looks to evaluate the changes in performance trends of marine hydrokinetic arrays when in an open system versus systems with distinct bathymetries.

Currently array performance has been primarily discussed for an open channel or for a channel with a flat bottom. The studies have shown that array performance will increase up until a specific point as distance between devices in the downstream direction increase. This pattern occurs because each device after the first row of devices with in an array is in the wake of the preceding devices. The power produced from a MHK device is directly related to the cube of the flow velocity. The greater the downstream distance between devices the more time the wake will have to recover. After enough distance the wake will reach a maximum recovery point and any additional distance between adjacent devices will not affect the inflow velocity. Increasing the distance between each device also increases the required foot print for an array. In real deployment locations the array size is limited to a regulated footprint, so spacing becomes an optimization problem. Real world locations can also are complex domains that are irregular in shape and have the potential to impact flow through and around the arrays. The question driving the research behind this thesis is "Does the trend for array performance stay the same over different bathymetries?" If the trend for performance stays the same, each array would perform the same relative to each of the other arrays. This would mean that developers could optimize and array within an open channel then adapt that array into any real world site. If the trends do not hold constant, then each array must be optimized for each localized deployment location. The research presented in this thesis looks to answer that question. Numerical modeling was used to simulate and test arrays of current-energy-converters. Over 60 simulations were completed to analyze the effects of bathymetry on array performance.

Contribution

This thesis makes three principle contributions to the field of MHK arrays. The results of this thesis show that:

1. The bathymetry of a deployment location has the potential to drastically change the performance properties of CEC arrays.
2. Array configurations developed in an open channel will not demonstrate the same trends of performance within more complex bathymetries.
3. Arrays can be categorized similar to individual devices by adapting actuator disk theory to arrays. This results in array coefficients for thrust and power that can be used to compare arrays over a wide range of bathymetries.

Thesis Outline

This thesis is broken up into eight chapters: Introduction, Background, Marine Hydrokinetic Design, Methodology, Calibration, Arrays Within an Open Channel, Arrays Over Sloped Bathymetries, and Conclusion. The background in the following chapter provides an overview of wind energy, types of marine hydrokinetic energy, types of energy converters, and challenges using marine hydrokinetic energy. The Marine Hydrokinetic Design chapter provides an overview of principles of device performance, MHK device layout, experimental test methods and numerical models. The Methodology chapter shows the process used to test arrays over different bathymetric layouts. The Calibration chapter discusses the calibration of numerical model parameters to experimental data and properties used in the later chapters discussing array simulations.

The Reference Bathymetry chapter covers all the parameters of linear arrays in open channel flow and creates a baseline for all of the bathymetric cases. The Bathymetry chapter discusses the results of array performance over two bathymetric domains and three distinct arrays. The Conclusion summarizes the finding and discusses the effect on developers and future research.

BACKGROUND

This chapter investigates the multiple forms of marine hydrokinetic energy and similar forms of energy. First wind energy is discussed as it is a building block for MHK current energy converter technology. Second, current energy is presented as one of the major sources for MHK energy. Third, wave energy is discussed as it is the largest source for available energy for MHK applications. Fifth conventional hydropower applications are discussed. The last section covers the challenges of deploying MHK devices in water.

Wind Energy

The fundamentals of marine hydrokinetic power are very similar to wind power. Both forms of power generation extract kinetic energy from fluid flow and convert it into mechanical energy that is then converted finally into electrical energy. In particular, current and tidal devices operate in much the same way that wind turbines do. Wind power most commonly uses horizontal-axis wind turbines (HAWT) and vertical-axis wind turbines (VAWT), or cross-flow turbines, to capture kinetic energy. Marine current energy converters used initial designs based off of their wind counter parts. As the marine hydrokinetic industry leverages knowledge from wind, it is important to understand the advantages, disadvantages, and types of wind devices.

The wind energy is appealing because it does not require any burning of fossil fuels and there is no monetary charge to obtain wind. Wind will always exists as long as pressure and thermal differences occur over the Earth’s surface; which means that wind will always be a viable energy resource. The only gas emissions occur during manufacturing, transportation, and potentially maintenance. The foot print taken up by wind energy devices is also not always intrusive, because the land below the turbines can also still be utilized, unless deployed over the coast. This means that it is relatively easy to access turbines for maintenance purposes and it is possible to still use the land for other purposes such as agriculture. However, as with any energy source, there are drawbacks.

Wind itself is very unpredictable, which makes consistent production of energy problematic (Wan 2002). Annually a wind farm will produce a fairly constant amount of energy, but during the year it is difficult to predict the occurrence of wind (Wan 2012). This means that the wind energy must be supplemented by another energy source for constant power generation. Some wind farms, like the Judith Gap Wind Farm in Montana, are in remote locations and are producing more electricity than is consumed (WRA 2015). The infrastructure does no exists to transport the electrical energy from the remote sites to more populated areas. It is possible to develop this infrastructure, but it is costly. There is potential to store the energy within battery banks (GE 2015). However, modern energy storage methods are not effective enough to make wind a standalone energy source (Morgan 2014).

Wind turbines have an optimal range of performance based on wind speed. If the wind velocity is not in the ideal range the turbine will not operate optimally and minimal power will be produced. Environmentally there have been issues with flocks of birds colliding with wind turbine blades, because of poor visibly of spinning wind turbine blades (Anderson et. al. 1999). Noise pollution is a potential problem that is dependent on the type, size, and number of wind turbines (Rogers et. al. 2006, Roadman & Huskey 2013). It is difficult to find optimal material for wind turbine blades. Modern wind turbines are made from composite materials in order to optimize weight and performance. Without precise manufacturing techniques and intensive quality control, which requires time and money and can dramatically increase the levelized cost of electricity, the performance of the composite materials decrease. This leads to the chronic problem of modern wind turbine blades not lasting their whole design life of approximately 20 years (Tawade et al. 2014). Over time moisture build up can expedite the degradation of the composite material (Miller et al. 2012). All these deficiencies factors into the cost of producing wind energy. The price of wind energy has drastically decreased over the past 30 years, but other sources such as oil and gas are still substantially cheaper.

Wind Turbines

The more efficient wind turbines are, the more cost effective wind energy can be. There has been a lot of research during the past 30 years on turbine design. Regardless of the design every wind turbine converts the kinetic energy of the wind to rotational energy used to drive a generator, either directly or through a gear box. These turbines can be designed to be driven by either lift or drag. Drag based turbines utilize the incoming flow to push scoops that cause the turbine to rotate; whereas lift designs use airfoil-shaped blades to generate lift, like an airplane, to drive rotational motion. HAWTs rotate about an axis parallel to incoming flow and VAWTs rotate about an axis perpendicular to incoming flow. Examples of these two types of devices can be seen in Figure 2.1. This means that HAWTs must be facing the flow direction in order to optimally generate power. On the other hand VAWT orientation does not matter as any inflow will still be perpendicular to axis of rotation. In the 1980s the wind industry chose to focus research and development on lift driven horizontal-axis wind turbines. Due to this direction there is currently more information available on HAWTs than VAWTs. This does not necessarily mean that HAWTs are better than VAWTs. Since the emergence of marine hydrokinetics, VAWT research has resurfaced (Ferreira 2009, Salter 2012, Sutherland et al. 2012). Some theorize that VAWTs can potentially be more beneficial than HAWTs when placed in arrays due to an increase in device density within a deployment footprint (Salter 2012, Sutherland et al. 2012).

(a) (b)

Figure 2.1: Wind turbines (a) horizontal axis wind turbine (Smith 2007), (b) vertical axis wind turbine (SNL 2015)

<u>Wind Turbine Components</u>

All wind turbines are made up using similar components. Every type of wind turbine consists of blades, rotor, tower, gear box, and generator. The blades are in the shape of an airfoil and are similar to those used on planes. Air flow over the blades cause a pressure differential generating lift and drag forces which results in a torque load on the rotor. The torque load causes the blade and rotor assembly to rotate. The rotor hub, to which the turbine blades are attached, is connected to a gear box or generator through an input shaft. The generator is used to convert the mechanical work of the turbine into electricity; which can be transferred to a power grid. Generators require specific shaft rotational speeds to convert the mechanical energy an optimal amount of electricity. The purpose of a gearbox is to bridge the rotational speed gap between the rotor and the generator. The gearbox is not always required as some turbines are designed to rotate at the optimal speed for the specified generator, a direct-drive setup. Some of the more complex wind turbines use a break to slow the rotation of the rotor assembly when wind gusts might cause the turbine to rotate faster than the optimal rate. Every turbine has a nacelle; which is used to attach the rotor assembly to the tower and contains the generator, gearbox, and electrical components. The tower supports the nacelle off the ground. Some horizontal-axis wind turbines have a yaw drive that is used to orientate the nacelle and rotor assembly on top of the tower to directly face incoming wind. An anemometer can be used on or near the wind turbine on a MET tower to send wind direction information to the turbine.

Turbine Arrays

The current generation of HAWTs are capable of producing multi-megawatts of power (Siemens 2015). However, even a multi-megawatt turbine by itself does not produce enough power to be economically feasible; which is why wind farms exists.

Wind farms are a collection of wind turbines deployed at a single location. Figure 2.2 shows an example of a wind farm in the state of Montana. Individual MHK devices also do not generate enough power, unless quite large, to be economically viable and need to be deployed in arrays. Usually wind farms consist of a couple hundred wind turbines. When this many devices exist in one location the performance of each device will be dependent on its location within the array. Consider a couple of rows of turbines where each row is perpendicular to incoming flow. The first row experience uninterrupted flow and will have the most potential for power production. Dependent upon the spacing between rows, the second row experiences the decreased flow velocity caused by the first rows extraction of energy. Power is directly related to the fluid velocity cubed. Therefore, the amount of power generated by the second row is limited to the average velocity of the fluid after moving through the first row. This pattern continues for each proceeding row. There are fundamental questions concerning proper placement of devices within arrays to optimize power production and also for other factors such as device and infrastructure costs, and environmental impacts. Researchers have begun to investigate optimal internal device spacing for wind farms (Archer, et. al. 2013, Yang et al 2013, Stevens et al 2015). In the marine hydrokinetic world there are even more concerns dealing with naval navigation, and recreation uses.

Figure 2.2: Judith Gap wind farm (Lehman, K., photo by D. Morris)

Current Energy

Marine hydrokinetic current energy is very similar to wind energy. Both forms of energy convert kinetic energy from fluid flow and convert it into electrical energy. Current-energy-converters (CECs) are used to capture the kinetic energy from water currents and convert it to electrical energy. The present generation of CEC devices are cross-flow and horizontal-axis water turbines, very similar to wind turbines. Georgia Tech completed an assessment of energy production in the continental U.S. for these three forms of marine hydrokinetic energies and found that current energy has the potential to provide 533 TWh year^{-1} of energy (Haas et al. 2011, EPRI 2012). Alaska also has potential for large amounts of energy generation, but most the sources are distant from populated areas which makes energy transport difficult and expensive. There are three predominant sources for current energy: ocean, tidal, and riverine.

Ocean Currents

Ocean currents are defined as the continuous flow of water in the ocean at a specific direction. There are many different types driving forces for ocean currents and not all currents are driven by the same forces. These forces are known to be caused from the Coriolis Effect, gravity, wind, temperature, pressure gradients, density gradients, tides, river discharge, and bottom friction (Haas et al 2013). Tidal streams can technically be defined as ocean currents; however, they are classified separately for MHK purposes due to the predictability of the driving forces and average operational depth. Ocean currents, apart from tidal, are not always continuous year round and difficult to predict. Around the U.S., the Gulf Stream along Florida to North Carolina has the potential to produce 163 TWh $year^{-1}$, and is the main focus of ocean current energy in the U.S (Haas et al 2013). The gulf stream is a surface current that is driven by winds from Africa across the Atlantic Ocean to the North American coastline, at which point it is redirected North due to the continental boundary. Other ocean currents exists, but have not been characterized for potential power availability. The advantages of ocean current energy are the relatively short distance to shore, minimal pollution during operation, and no cost in acquiring of the working fluid.

Tidal Streams

The resource assessment done by Georgia Tech defines tidal streams as "high velocity sea currents created by periodic horizontal movement of the tides, often magnified by the local topographical features such as headlands, inlets to inland lagoons, and straits" (Haas et al 2011). Tides are the rising and falling water height in the ocean caused by the gravitational effects of the moon and sun acting upon Earth. Tidal patterns are fairly predictable due to the constant astronomical effects. NOAA also has over 2,700 tidal current stations in the U.S. that can be used to predict tidal flows. Tidal currents can be utilized in many parts of the U.S. coastline, such as Knik Arm, AK; Tacoma Narrows, WA; Golden Gate, CA; Muskeget Channel, MA; Western Passage, ME; Puget Sound, WA; New York, Connecticut; Cook Inlet, AK; and Southeast Alaska (Haas et al 2011). There are also quite a few locations around the world including Europe, Japan, and Canada. According to the "Assessment of the Energy Production from Tidal Streams in the United States" report, the available recoverable energy for tidal streams to be 250 TWh $year^{-1}$ (Haas et al 2011). Remote coastal communities can also benefit from tidal power as they would no longer have deal with the transport of fossil fuels.

River Currents

Any river that has a high volumetric flow rate can potentially be used to power CECs. The largest rivers of interest for power production in the continental U.S. are the Mississippi, Missouri, and Illinois. Sandia National Labs completed a study on part of the Mississippi for potential CEC deployment locations (Roberts et al 2012). In Alaska there are many possibilities for riverine power; such as the Yukon, Kuskokwim, Koyukuk, and the Copper Rivers. Out of the three sources of current energy, riverine has the least potential for energy production, but is also the easiest type of marine hydrokinetic energy to access. River height and flow rates change seasonally, but are still regularly predictable throughout the year. The Assessment and Mapping of the Riverine Hydrokinetic Resource in the Continental United States report states that the available kinetic energy potential from rivers in the continental U.S. is approximately 120 TWh year^{-1} and even more in Alaska (EPRI 2012).

Wave Energy

Wave energy is similar to current energy in that it extracts the kinetic energy from the water, but it is done in a much different way. The principal waves of interest are caused by the transfer of energy between wind and the ocean causing an oscillating motion of energy. The size and duration of a wave is determined by the fetch, distance the wind blows, and the length of the wind gust. Because wind is a direct cause of waves, it is often difficult to predict when wave will occur and the size of the waves, but as with ocean currents and the seasonality of rivers, probability distributions of wave height, length, and direction exist. Wave-energy-converters capture the kinetic energy from the waves and transform it into electrical energy. There are many types of WEC devices: the attenuator, point absorber, oscillating wave surge converter, oscillating water column, overtopping/terminator device, submerged pressure differential, bulge wave, rotating mass, etc. (EMEC 2015). The predominate WEC devices are attenuators and point absorbers. The Pelamis Wave Energy Converter was the world's first offshore wave energy converter to generate electricity to a power grid and is an example of an attenuator, Figure 2.3. The device consists on many subsections which use hydraulic cylinders actuated by the wave motion to drive a motor. The point absorber is the other main type of WEC and acts like a buoy. The motion of the waves causes the point absorber to oscillate up and down which drives a generator that is used to generate electricity. Wave energy in general has much larger potential for electricity generation then current energy. According to the Mapping and Assessment of the United States Ocean Wave Energy Resource Repot the available recoverable energy potential for waves is approximately 1,170 TWh $year^{-1}$ (EPRI 2011).

Figure 2.3: Pelamis wave energy converter (EMEC 2015)

Conventional Hydropower

Nearly all power generated from water until recently was due to a buildup of potential energy that is then released as kinetic. This is the fundamental difference between marine hydrokinetic energy and conventional hydropower. In Conventional hydropower dams are used in conjunction with levees/flood gates to generate electricity. Dams block flow causing a buildup of water head. The higher the head the more potential energy is gathered into the system. Water can be released at the bottom of the dam using the channel height, or head, to accelerate flow through a turbine. Even though conventional hydropower is different from marine hydrokinetic there are cases where both forms of energy are similar. In the case of a tidal barrage a dam is created off the coast. As the tides come in the water flows contained area building head pressure. After high tide the dam is closed off using sluice gates. The water is slowly released back through turbines using the difference in water head from the high tide reservoir to the low tide along the coast to generate power. Even though marine hydrokinetics have been within the last decade, tidal barrages have existed since the 1960s.

Challenges of Submersion

The Marine Hydrokinetic Industry is still in its infancy so much of the information about device performance and array performance is built off of the foundation developed by the wind industry. Transitioning from wind to water is much more complex than changing the working fluid. There are changes in flow predictability, device survivability, potential impact on recreational boating and shipping routes, environmental concerns, and bathymetric effects.

Designing CECs for water is very similar to wind from a standpoint of fluid mechanics. From a macro perspective the water is more viscous, dense, and flows slower than air which results in increased forces acting upon the CECs. The physical loads in water are drastically larger than in wind and impact design. Due to the increase in loading MHK turbine blades are generally smaller than their wind counter parts. Being submerged in water also introduces other factors that influence device life; such as faster aging, surface fouling, and organic growth (Bunn & Yokochi 2014). Modern wind turbine blades are made out of composite materials to maximize weight and performance. When submerged in water composite materials degrade much faster when than when above the surface, and salt water can be even more damaging (Miller et al 2012). There is also algae and other organic growth that will tarnish the surface of a water turbine. Researchers are attempting to find coatings that inhibit growth (Bunn & Yokochi 2014). If no coating proves effective then a maintenance schedule must be put into effect just to clean the surfaces of the devices. Maintenance can be very problematic for MHK turbines depending on the depth and how close to shore the devices are located. In the wind industry all of the turbines are above ground and relatively easy to approach. It is also easy to visually see and inspect wind turbines. On the other hand, MHK turbines are all located underwater which brings up many questions for maintenance: can the turbine be repaired under water, can the turbine be raised to the surface for repairs, can the turbine be brought to shore, how far away from the shore is the facility that does repairs, and what techniques can be applied for preventative maintenance? These are questions that developers for CEC and WEC need to have answers for before deployment.

The deployment of MHK devices also has the potential to greatly impact the local environments (Cada et al. 2011). Little is known how these devices will impact underwater ecosystems. Research is being conducted for device interaction with various species and schools of fish (Viehman & Zydlewski 2015). Researchers have also used numerical models in an attempt to predict blade strikes (Romero-Gomez & Richmond 2014). Even sea lion interactions with MHK turbines is being observed (Tomichek et al 2014). Noise pollution from MHK devices also have the potential to impact native marine life and is being investigated (Patricio et al 2009). Most researchers are not worried about single device effects on ecosystems, but are concerned about arrays of hundreds of devices. As the MHK industry is relatively new it is difficult to gather empirical data and access all of the potential impacts.

Experimental Marine Hydrokinetic Turbine Testing

Presently only a small number of individual MHK devices are in operation with a deficit of available performance data for arrays. Research is ongoing to determine the most effective ways to model individual turbine/device performance using small-scale tests in flumes and computational fluid dynamics (CFD). Flume experiments have shown CEC wakes having velocity deficits near 60% immediately behind the device and propagating 15-20 device diameters downstream before recovering to approximately 90% of the free-stream velocity (Batten et al. 2013, Neary et al. 2012). Two issues with flume experiments are the relatively large blockage factors and turbulence scaling. Blockage is defined by area ratio of device surface area to cross-sectional area of the channel. From a fluid mechanics perspective the conservation of mass dictates that a decrease in flow area will lead to an increase in velocity. The walls of the flume will cause flow acceleration effects unless sufficiently wide; which is the fundamental flaw of a flume. In actual channels, blockage ratios are most likely small or seemingly nonexistent for deployments of fewer than a hundred devices. The open-water measurements appear to indicate a faster recovery due to higher turbulent mixing (James et al. 2011).

It becomes costly and potentially difficult to manufacture and test arrays of devices. This has forced researchers to find new ways to experimentally model turbines. Researchers have recently discovered that porous disks can be used to represent horizontal-axis turbines with good results as they capture thrust loads and velocity fields well (Harrison et al. 2009, Yang et al. 2013, Crasto & Gravdahl 2008). The porous disk also have similar wake expansion to a horizontal axis turbine when the diameter and thrust coefficient match that of the turbine (Lignarolo et al. 2015). It has also been shown that porous disks represent turbines well if the turbulence of the flow is properly quantified (Blackmore et al. 2014). However, porous disks are not able to replicate the turbulence and vortex wake accurately or immediate wake, one to three device diameters downstream. The advantages of porous disks are in ease of manufacturing and instrumentation during experiments and the highly decreased numerical computational costs when compared to a small scale CEC/MHK devices. This becomes important when analyzing large arrays or domains as computational cost drastically increase to appropriately capture the shear stresses on the rotating blades.

Numerical Modeling Marine Hydrokinetic Turbine

The Navier-Stokes equations govern the behavior of fluid flow. These equations are broken down into various forms to solve fluid dynamic problems. The Navier-Stokes equations can be broken down in terms of conservation of momentum, energy, and mass. If the domain and geometries are relatively simple, then it is possible to use basic Continuity, Bernoulli's, and Momentum to model fluid flow. The simplistic methods work well until solid body motion is added or the domain geometry becomes relatively complex. At this point numerical simulation is required. There are two types of formulations that are used in CFD, Eulerian and Lagrangian. The Eulerian methods primarily use finite volume methods, finite element methods are also used, to create a discretized fluid domain. How the fluid domain is discretized will depend on the order of the simulation and what cell/mesh shapes are being utilized. The Lagrange particle method does not require the discretization of a whole domain as it tracks the individual fluid particles.

There are many variational break downs of these numerical models used in MHK turbine analysis: large-eddy simulation, Reynolds Averaged Navier Stokes, Blade Element Momentum, Vortex Particle Method, and other hybrid methods. When modeling MHK/CEC devices the fluid flow is generally considered to be fully turbulent due to the device interaction with the water and the flow conditions of deployment domains.

The Blade Element Momentum (BEM) method uses linear-momentum and blade element theory to determine the thrust and torque loads on a turbine; however, it provides no details about the wake behind a device or multiple-device interaction and is pseudo two-dimensional. Momentum is balanced in a rotating annular stream tube that is pathed through a turbine. The forces on the blade elements are evaluated by known tabulated lift and drag coefficients. Blade-element momentum solvers run in fractions of a second, and are therefore much faster than RANS or LES and are regularly used for designing horizontal-axis turbines and determining their performance (Mozafari 2014). However, there is no commercially available CFD programs that applies BEM to cross-flow water turbines with reasonable accuracy. The largest drawback to the BEM method is that other methods such as LES and RANS yield more accurate results and BEM has not been demonstrated to work for arrays.

Vortex methods are mesh-free Lagrangian particle methods that propagate vortex nodes, line-bodies, and/or sheets from upstream structures (Sale et al. 2014). This allows turbine performance and wake structure to be analyzed at a computational cost lower than RANS, but higher than BEM. In vortex models turbine blades are segmented into sections which are represented by a bound vortex. Vortices are shed from the blade when the turbine rotates due to the change in bound vortex strength. Sandia National Laboratory has developed a Code for Axial and Cross-flow Turbine Simulation (CACTUS) and can include simple bathymetry and free-surface effects (Murray 2011).

The large eddy simulation (LES) is a high order numerical approximation of the Navier-Stokes equations used to simulate turbulent flows. It was first developed in the 1960s to simulate atmospheric air currents and since has been adopted to solve a variety of other flows. LES has the capability to capture turbulent structures down to the smallest mesh size; which provides some of the best detail in wake structure and device-turbulence interaction (Yang et al. 2013). Many research groups are using LES simulations to model wind farms and MHK devices (Sotiropoulos et al. 2011). The drawback of the LES lies in the computational costs; which usually requires a cluster or super computer to run the analysis over multiple days to weeks, depending on the simulation.

Perhaps the most widely used CFD solver is the Reynold's Averaged Navier-Stokes (RANS) model. The RANS model is based off Reynolds Decomposition; which is used to separate the time-averaged and fluctuation quantities of the Navier-Stokes equations. The model does not discretely resolve the turbulent structures like LES, but instead averages the stresses; which makes the method less computationally intensive than the LES. However, it is still much more computationally expensive than the BEM.

There are methods that combine different methods into hybrid models. The software package Star-CMM+® has a discrete eddy simulation (DES) method that combines RANS with LES. A hybrid model combing LES and vortex line-bodies has recently been developed for wind turbine applications to capture turbulent wake mixing and interaction within an array in a more computationally efficient manner (Churchfield et al. 2012).

TURBINE DESIGN

In order to successfully evaluate MHK array designs, individual device must be understood. The information presented in this thesis does not apply to wave-energy-converters. This thesis will explicitly focus on current-energy-converters. Different array simulations would need to be run to model WEC devices. Similar to the wind industry the primary CECs used in MHK applications are horizontal-axis-water turbines and cross-flow turbines. In this section the design parameters of CECs and arrays will be discussed followed by experimental testing and numerical modeling of the devices.

Actuator Disk Theory

Regardless of the type of CEC each type of turbine follows the same general principles; which means performance characteristics of a CEC can be evaluated using actuator disk theory. Actuator disk theory evaluates fluid flow through a turbine as if it were inside a stream tube and incompressible. A stream-tube is a collection of streamlines that lie within a boundary surface and do not interact with flow outside the boundary. The turbine extracts kinetic energy from the fluid flow causing the flow to slow down. In actuator disk theory the energy extracted is in the form of momentum loss. The velocity is assumed to gradually decrease through the stream-tube so that it has already slowed by the time it reaches the turbines. The flow after the turbine in the wake is much slower than the initial flow and at a lower pressure. In reality, the flow of the wake proceeds farther downstream from the turbines the flow will begin to recover and eventually reach an equilibrium state. Figure 3.1 shows a visual representation of a stream tube and a cross-sectional cut out relating velocity, *U*, pressure, *P*, and area, *A*, at different sections within a stream tube.

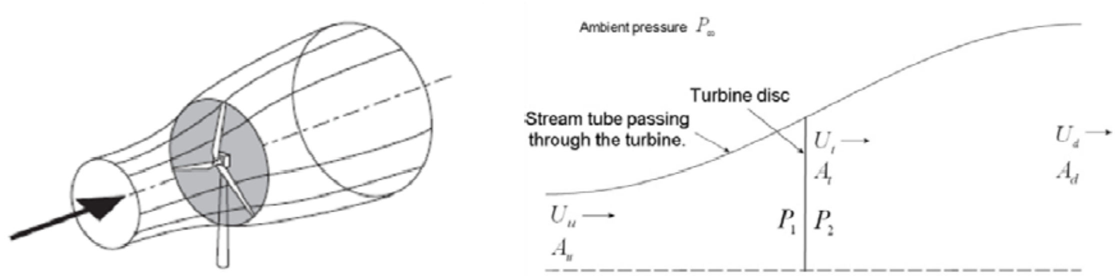

(a) (b)
Figure 3.1: Actuator disk visualization (a) visual representation of a stream tube (Burton 2011), (b) representation of the cross-section of a stream tube. (WPP 2015)

The actuator disk model can be used to calculate the theoretical power output of a generalized turbine based upon continuity and linear momentum theory. Hydrokinetic power generation is a function of upstream velocity, U_∞, water density, ρ, cross-sectional area of the MHK device, A_D, and a velocity-dependent coefficient of power, C_P. Power can also be related by an axial induction factor, a. The axial induction factor relates upstream velocity to velocity at the turbine plane, U_D.

$$U_D = U_\infty(1 - a) \tag{3.1}$$

$$Power = \frac{1}{2}\rho A_D {U_\infty}^3 C_P = 2\rho A_D {U_\infty}^3 a(1 - a)^2 \tag{3.2}$$

$$C_P = \frac{Power}{\frac{1}{2}\rho {U_\infty}^3 A_D} = 4a(1 - a)^2 \tag{3.3}$$

The thrust in the flow-direction can similarly be calculated by

$$Thrust = \frac{1}{2}\rho {U_\infty}^2 A_D C_T = 2\rho {U_\infty}^2 A_D a(1-a) \tag{3.4}$$

where C_T is a velocity-dependent coefficient of thrust (Burton et al. 2011). The coefficient of thrust, C_T, is the non-dimensionalized force on the device caused by the pressure drop across the plane of the rotor and the shear on the blades relative to the available kinetic energy in the flow.

$$C_T = \frac{Thrust}{\frac{1}{2}\rho {U_\infty}^2 A_D} = 4a(1-a) \tag{3.5}$$

The coefficients of power and thrust can also be related to each other through the axial induction factor.

$$C_p = C_T(1-a) \tag{3.6}$$

And absolute power can then be related to thrust through the upstream velocity and the axial induction factor.

$$Power = Thrust * U_\infty(1-a) \tag{3.7}$$

Therefore an increase in thrust on a turbine can be used as a surrogate for an increase in power production, even if the turbine is not generating optimal power, and up to momentum theory limits. The power of a turbine is limited by the Lachester-Betz limit. The maximum coefficient of power can be found by taking the partial of the coefficient of power with respect to the axial induction factor.

$$\frac{dC_P}{da} = 4(1-a)(1-3a) = 0 \qquad (3.8)$$

Maximum power is achieved at the Betz limit, when a = 1/3 and C_{PMAX} = 16/27 or 0.593. The actuator disk model is a general representation so it applies for all types of turbines regardless of device design. It is important to note that turbine power production is directly related to the cube of the inflow velocity. The inflow velocity will be site specific and a small change in the inflow velocity will have a large effect on the power production. This is extremely important for array development. The first row of devices will have an optimal power output, but each proceeding row will experience the wake of the forward devices. The velocity of the water decreases each time it flows through a row of devices. This is the fundamental reason of why array layouts are important and need to be considered when deploying many devices.

Design Parameters

Even though the actuator disk model only takes into account general turbine design, the Betz limit still applies to all wind and water turbines. Wind and water turbine designers attempt to make turbines that operate at as close as possible to this limit. Optimal device designs really on specific analysis of device dependent parameters: type of turbine, tip speed ratio, hydrofoil shape, solidity ratio, twist angle, chord length, and thickness of the blades.

Tip Speed Ratio

The tip speed ratio (TSR) is a non-dimensional term used to relate the rotational velocity of the turbine to the inflow velocity of the turbine. It is a function of angular velocity, ω, inflow velocity, u_0, and the radius, R, of the turbine. Equation 3.9 shows this relation in analytical form. The coefficient of power for a turbine can be directly related to tip speed ratio. Every turbine will have a curve relating tip speed ratio to coefficient of power. Ideally each turbine will operate at the maximum coefficient of power, but is not always the case as wind and water speeds are subject to change. Variable speed water and wind turbines were developed to be able to operate efficiently over a range of inflow velocities.

$$TSR = \frac{\omega * R}{u_0} \tag{3.9}$$

Foil Geometry

The purpose of wind and water turbine blades is to generate lift to cause the rotational motion of the rotor. Lift is caused by the pressure differential across the surface of the turbine blade. The pressure differential is caused by the effect that the shape of the airfoil/hydrofoil has on working fluid. The foils are designed so that when fluid flows over the blade there is a high pressure zone under the blade and a low pressure zone over the blade. The pressure difference induces a lifting force on the blade which in turn causes the rotational motion. Hydro/air foils are characterized by chord length, blade thickness-to-chord ratio, maximum thickness, camber, twist, leading edge profile, and trailing edge profile. Figure 3.2 shows a geometric layout of an airfoil. Chord length is defined as the linear distance from the front of the leading edge to the end of the trailing edge. As seen in Figure 3.2 the thickness of the foil changes over the length. This is called camber and is the asymmetry between the surfaces of a foil. The camber line is like the chord but runs through middle of the blade from the leading edge to the trailing edge. The camber of the foil can be used to dictate the pressure differential of the flow. Air/hydrofoil coefficients of lift and drag are characterized by Reynolds number and angle of attack. Reynolds number is the non-dimensional ratio of inertial to viscous forces, equation 3.10. The inertial forces are in terms of density, ρ, velocity, u, and length, L. For an airfoil the chord length is used for L.

$$Re = \frac{\rho u L}{\mu} \tag{3.10}$$

Angle of attack is the angle from the chord line to the incoming flow vector as is seen in Figure 3.2. For turbine application angle of attack is also regarded as blade pitch. Changing the angle of attack effects the pressure distribution over a foil. Coefficients of lift and drag can be plotted for a specific foil shape versus angle of attack at different Reynolds numbers. When considering one fluid the Reynolds number is directly proportional to the velocity of the fluid, because the density and dynamic viscosity are the same. Turbine designers can use these charts to select foil geometries that operate well for specific Reynolds numbers based on inflow velocities. The last property of a foil is the angle of twist. Wind and water turbines have twisted blades due to the change in tip speed ratio over the blade length. Equation 8 shows that the TSR changes depending on the radius of the blade. The outer edge of the blade moves faster than the inner sections of the blade. Turbine blades are twisted so that through the length of the blade each section experiences the same tip speed ratio and angle of attack; thus creating a uniform lift and drag profile along the length of the blade.

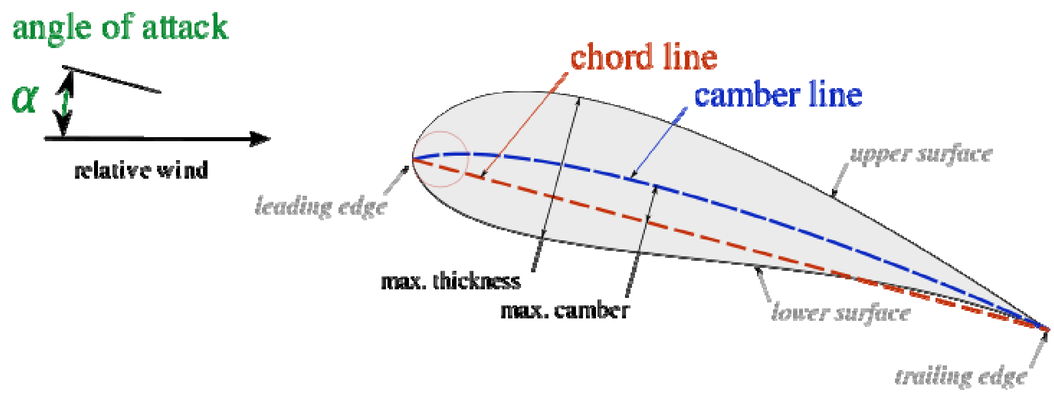

Figure 3.2: Characteristics of an airfoil (Cleynen 2011)

Solidity

Solidity is defined the ratio of the swept area, or the area that the blades pass through, to the area occupied by the blades. The solidity of a wind or water turbine effects the tip speed ratio versus coefficient of performance curves. Low solidity values results in a performance curve that does not vary much over a large tip speed ratio range. The drag forces are high for low solidity turbines; which results in a low maximum coefficient of performance and higher starting torques. Lower solidity turbines provide the most consistent power generation in areas where the annual changes in flow velocity are substantial. High solidity turbines have a narrow performance curve with a distinct coefficient of performance. These turbines are very sensitive to changes in tip speed ratio. High solidity turbines are optimized for use in locations where the flow velocity is fairly constant. The solidity can become too high where stall loses dominate and the coefficient of performance is extremely low. The solidity of a turbine can be tuned through chord length and number of blades and is often categorized in terms of chord solidity, $\sigma_{R,}$; which is the ratio of the number of blades, B, and chord length, c, to the circumferential length, $2\pi R$, equation 3.11.

$$\sigma_R = \frac{B * c}{2\pi R} \qquad (3.11)$$

Number of Blades

The number of blades is proportional to the solidity of a wind or water turbine. There is an optimal amount of blades for each type of turbine. The tradeoff for optimization can be seen in equation 3.10 and is dependent on chord length and number of blades. Increasing the number of blades alone does not mean there will be an increase in power production as there is an increase in solidity. If the number of blades is increased the chord length of the blades must be decreased to operate at an ideal solidity. The problem with the larger number of blades lies in the cost of turbine blades. A five bladed turbine with a smaller chord length may be more efficient at capturing energy; however a three bladed turbine can potentially be more cost effective to build and repair. This is why most horizontal axis wind turbines only have three blades.

Marine Hydrokinetic Array Layouts

Like many other parts of MHK developments much of array design is built off knowledge gained through the wind industry. Researchers for the wind industry have evaluated wind farm performance for a variety of device placements. The majority of research that has been conducted assumes that each wind turbine is identical. This includes turbine height; which means all of the turbines operate at the same distance above the surface. For the purposes of this thesis, the flow direction will be defined as the longitudinal direction and is perpendicular to each row of the array. Each row is in the lateral direction. Columns of turbines are parallel to the inflow in the longitudinal direction. Figure 3.3 demonstrates the terminology used to in this thesis to discuss array layouts.

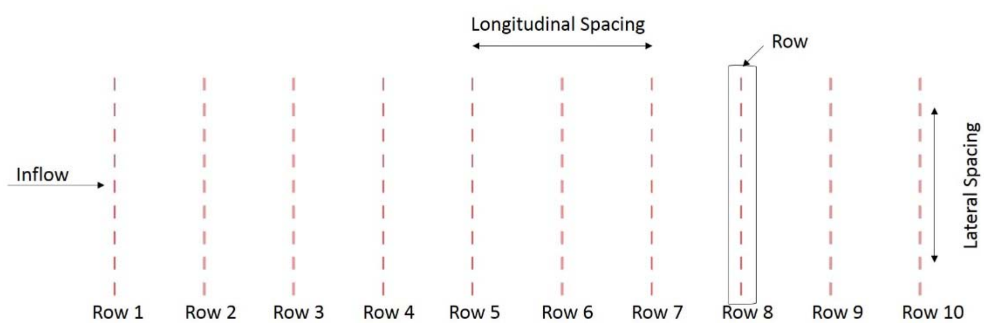

Figure 3.3: Array spacing diagram

The most common types of array layouts are linear-grid, staggered-grid, and triangular grid. In a linear-grid the turbines are placed into rows and columns; with one device located on either side of the inner turbines. Figure 3.4 (a) shows the layout of MHK devices in a linear-grid. Staggered-grids were developed as a way to more efficiently deploy turbines. In a staggered-grid the first row of turbines is the same as the linear-grid, but the second row is offset laterally so that each turbine is no longer directly behind, but in between the turbines of the first row. The second row is no longer directly in the wake of the first row which means that the second row of devices will experience higher velocity flow than its linear grid counterpart. The third row is then laterally spaced so that it is behind the first row and the fourth row is behind the second. The staggered grid is essentially doubling the longitudinal space between rows, thus doubling the length the wake has to recover between rows. Figure 3.4 (b) shows an example of a staggered-grid array. Research has shown that there is flow acceleration around CEC devices. It is possible to use that increase in flow velocity in influence performance of the devices in proceeding rows (Myers and Bahaj 2011). Myers and Bahaj completed a range of experiments to investigate device performance and array spacing using porous actuator-disks in single and 2-3 device array layouts and demonstrated the effect of lateral spacing can either increase the thrust loads on adjacent devices or be used to accelerate flow between them. In a staggered grid the flow that is accelerated by the upstream turbines is in line for the subsequent row of turbines. Research has been done in an attempt to quantify the exact lateral and longitudinal spacing to maximize this effect (Churchfield et al 2012, Stevens et al 2014). Triangular-grid arrays operate on the same principle of trying to maximize the velocity at each turbine. The first row has n-number of turbines; where n is an arbitrary number. Each subsequent row has n+1 turbines, staggered from the previous row, and is longer in the lateral direction. The idea behind triangular grid arrays is to always have two additional turbines in each row that is unobstructed by forward devices. The triangular-grid array can also benefit from the acceleration of flow around the upstream devices in the same way staggered-grid does. Figure 3.4 (c) shows an example of a triangular grid array. When choosing an array scheme it comes down to an optimization scheme.

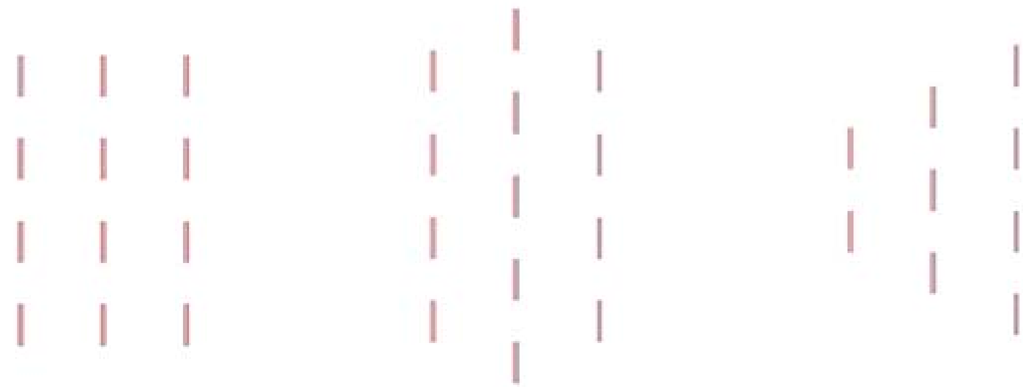

(a) (b) (c)

Figure 3.4: Array grids (a) triangular-grid, (b) staggered-grid, (c) linear-grid

Regardless of the layout each array configuration follows the same principles. The first row of devices, perpendicular to incoming flow, experience uninterrupted flow and have the most potential for power production. Each additional row is in the wake of the forward devices which reduces the amount of available kinetic energy. Research has been done to determine optimal of upstream to downstream device spacing (Yang et al. 2013). By using a staggered-grid the rows only need to be spaced half this distance as each turbine is in the wake of the turbine two rows ahead. The device type can also affect array characteristics, where the spacing between vertical axis wind turbines can be decreased while improving performance and loading conditions, if they leverage the bluff-body shedding, similar to efficiencies gained in fish schooling (Whittlesey et al. 2010).

METHODOLOGY

CEC arrays will be deployed in an endless possibility of river and near-shore domains with differing bathymetric profiles. The goal for this thesis was to investigate some simple bathymetries to determine the how performance characteristics of an array change when moving from an open channel to one with a geometric bottom. A commercial CFD program, Star-CCM+®, was used to analyze arrays of porous disks in an unbounded flow and four bathymetric test cases. First, the physical parameters of the model were calibrated against an experimental setup of a 3 actuator-disk array. Second, a set of array configurations in a free-stream were simulated to provide a performance reference for unobstructed flow. Third, the same array configurations were modeled within three different bathymetries to determine their potential effect on array performance. The principal data of interest are the forces on the disks and the wake recovery profiles.

Array Layouts

Linear arrays were used as a baseline for the simulations. For this study the type of layout of the array was assumed to be unimportant, because the advantages and disadvantages of each layout would be shared among all the arrays. What is important is how the thrust loads and wake recovery change for a specific array when moved to a new location. The arrays were composed of 90 porous disks: 10 columns of disks in the flow direction (longitudinal) and 9 disks in each row across the flow direction (lateral). The disks shared the same parameters; 0.1 m in diameter, 0.01 m thick, and had a porosity of

0.48. These are the same size and shape of disk used by Meyers and Bahaj at the University of Southampton (Myers and Bahaj 2011). The linear array configurations were categorized by lateral and longitudinal spacing between the actuator disks. These distances were reported in non-dimensional length based on disk diameter, D. The arrays are referenced by their (longitudinal/lateral) spacing for the remainder of the thesis. The array (7D/3D) refers to an array with 7 disk diameter longitudinal spacing and 3 disk diameter lateral spacing between the centers of adjacent disks. Twenty array configurations were tested in an open channel bathymetry to establish a baseline set of array performance characteristics. Every combination of longitudinal spacing of 2D, 3D, 7D, 11D, and 15D and lateral spacing of 1.25D, 2D, 3D, and 4D were used. The thrust loads on each disk, velocity profile through an array, and the wake recovery are the main characteristics of interest. The array configurations were then tested over two bottom bathymetries to determine if and how bathymetric changes affect the array performance characteristics.

Bathymetry Test Cases

Three bathymetries were tested to determine if the geometry of the system would impact array performance. The first bathymetry, Bathymetry 0, represented an open channel that was used to establish a baseline for performance data. Simple sloping bottoms were implemented in the next two bathymetries. The second bathymetry, Bathymetry A, had a lateral sloping bottom, and the third bathymetry, Bathymetry B, had a longitudinal sloping bottom. The linear arrays were placed over each of the three bathymetry cases and thrust loads on the disks and velocity profiles were recorded.

The unbounded flow geometry, Bathymetry 0, is a rectangular fluid volume with a length of 34.00 m, width of 6.40 m, and depth of 4.00 m and is shown in Figure 4.1. The disks are located 20 device diameters from the inlet and are centralized in the width and depth directions. The domain is large enough that there are no affects from the boundary conditions on the flow around the disks and in the wake.

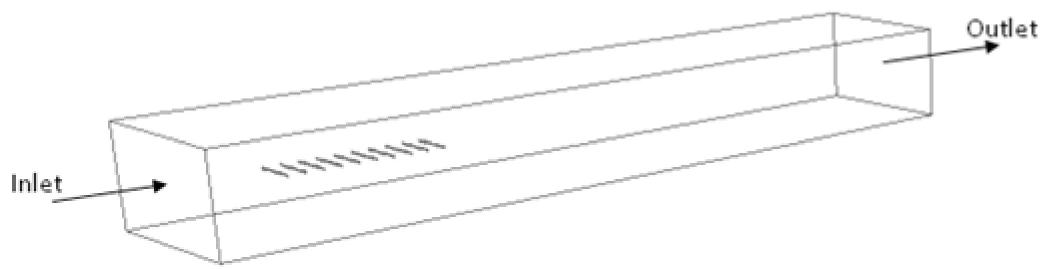

Figure 4.1: Open channel reference flow, Bathymetry 0

Bathymetry A, as seen in Figure 4.2 introduces a bed that is sloped laterally at 11.8° across the domain. The bed is sloped from one side of the volume, and positioned such that it is 0.1 m below the array on one edge to 1.44 m below the array on the other edge. This type of bathymetry can be used to provide a rough approximate estimate of potential close to shore locations; such as the sloping continental shelf.

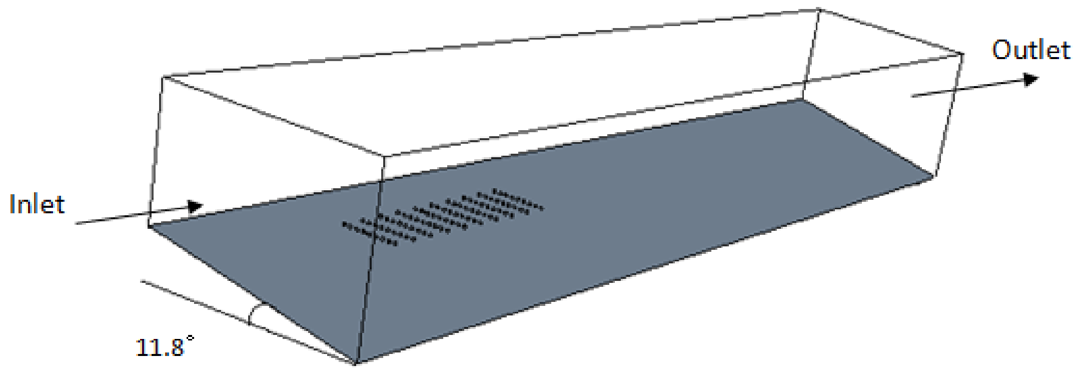

Figure 4.2: Bathymetry A

Bathymetry B has a positive sloping bed in the downstream direction, of 9.18° with a length of 10.03 m. The upstream and downstream depths are 4 m and 2.4 m, respectively. The performance characteristics of the arrays are subject to change depending on their location over the sloped bed. Two array deployment locations were used in Bathymetry B. The first deployment location placed the first row of the arrays at the beginning of the slope. The second location referenced the last row of the arrays to the apex of the sloped bed. Bathymetry B1 indicates Bathymetry B with the first deployment location and Bathymetry B2 for the second. In both cases the forward rows were deeper than the rear rows. This type of bathymetry has the potential to be seen in a river undergoing a vertical height change. The results for Bathymeries B1 and B2 are compared against each other and the open channel reference case.

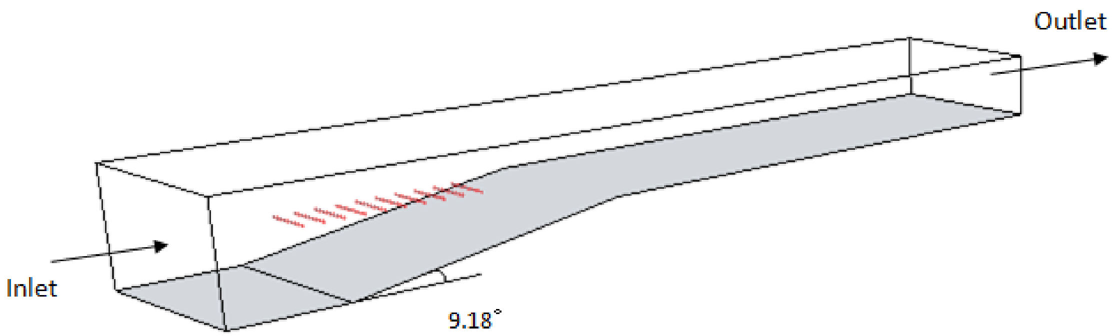

Figure 4.3: Bathymetry B1

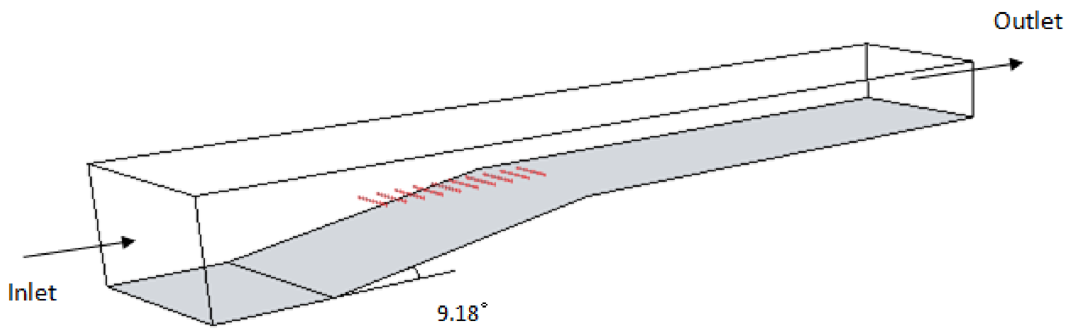

Figure 4.4: Bathymetry B2

Computational Fluid Dynamic Model

This thesis used porous disks to represent horizontal-axis-water-turbines. Porous disks are able to capture thrust loads and produce far wake profiles that are very similar to those seen in horizontal-axis-water-turbines (Harrison et al 2009). There is no rotational motion for a porous disk, so no vortex shedding or torque loads are produced. However, vortex shedding is a small contributor to the overall flow recovery behind a horizontal-axis-water-turbines. The model presented here assumes that the vortex shedding effect is negligible on the thrust loads and the downstream wake profile. No torque loads are present with porous disks so there can be no direct power generation; however, actuator disk theory can be used to relate the thrust loads on the porous disks to power by the upstream velocity through an axial induction factor, as was shown in equation 3.6. Therefore the thrust loads on the disks can be used as a surrogate for power generation.

Within a CFD model, porous regions can be used to represent iso- and anisotropic changes to the flow from inertial and viscous losses. These are treated as additional body forces and density ratios within the standard Navier-Stokes equations. Without sufficient detail from literature for the proportionality of these losses at different velocities, the porous disks were chose to be represented as packed beds. The Ergun equations solve for the viscous, P_v, and inertial, P_i, losses through (4.1, 4.2).

$$P_v = \frac{150\mu(1-X)^2}{X^3 D_p^2} \qquad (4.1)$$

$$P_i = \frac{1.75\rho(1-X)}{X^3 D_p} \qquad (4.2)$$

The dependent variables are the dynamic viscosity of the fluid, μ, density of the fluid, ρ, porosity, X, and mean particle diameter in the porous media, D_p, which was taken to be equivalent to the thickness of the disk. A calibration simulation was created to quantify viscous and inertial loses, diffusivity, and mesh and grid sizes, and is discussed in the calibration section.

The RANS solver for the Navier-Stokes equations was used to model the water flow through the porous disks and was chosen for it accuracy versus computational cost. The flow field was assumed to be fully turbulent and incompressible. This is a fairly accurate assumption as turbulent flows are expected in all deployment sites of full-scale devices and demonstrated within the literature compared against. The Spalart-Allmaras (SA) turbulence model was paired with the RANS model to represent turbulent flow structures (Spalart & Allmaras 1994). The SA model was chosen for its stability in a mixed porous domain and the diffusivity present in a mesh with various length scales. It is also less computationally expensive than the k-epsilon and k-omega equations or modeling with a large-eddy simulation, as there is only one equation to solve and mesh refinement is less critical near the boundaries. The SA turbulence model allows for parameterization of the turbulence diffusivity which is beneficial for scaling wake recovery. The flow field behind a disk can be experimentally modeled and the velocity recovery can be used to calibrate the SA diffusivity parameter in the CFD simulation.

The CFD model was calibrated using an experiment performed by researchers Myers and Bahaj in the Chilworth research laboratory at the University of Southampton (Myers & Bahaj 2011). This experiment used three porous disks to represent horizontal-axis-water turbines. The disks were positioned such that two disks were upstream of the third by three device diameters, which was centered between the upstream disks. The experiment was performed to see if the flow acceleration around the upstream disks could be used to increase velocity ingested by the downstream disk, and therefore increase the generated power. They were also able to quantify the wake recovery behind the disks. A numerical simulation of this experiment was created in order to calibrate the turbulence diffusivity, viscous and inertial loses of the porous disks, and relative mesh sizes.

Each simulation that was run used physical, mesh, and boundary parameters that were based off the calibration study of a 3 disk array. All of the simulations use the same physical parameters including inflow velocity, diffusivity, pressure, and temperature. The inflow velocity was $0.25ms^{-1}$. Standard atmospheric conditions were used for the pressure and temperature. Each array used similar mesh sizes in each area including around the disks and wake. The boundary conditions were the same across all the simulation with the exception of the bottom boundary in the reference channel. The bathymetry cases used a no-slip bottom boundary and the open channel reference study used a symmetry plane. Symmetry planes were also used for the sides and top of the domain. The side and top of the domain were sufficiently spaced so that there were no affects due to the boundary on the flow around the array.

CALIBRATION

Numerical models must be calibrated to real world experiments to produce the most accurate results. The Spalart-Allmaras turbulence model, within Star-CCM+®, requires the user to input a value for turbulence diffusivity. Without understanding the actual flow conditions and having measurements it is often very difficult to predict this input value. The best alternative to obtaining this value is to calibrate a numerical model of the same experiment. The user input value can then be changed until the numerical model best matches the experimental data. In this thesis the turbulence diffusivity needed to be calibrated against a real world experiment in order to have a physical grounding to be used in the study of arrays.

Experimental Tests

Researchers at the University of Southampton ran an experiment using a three porous-disks to model CEC devices (Myers and Bahaj 2011). This experiment was used to quantify the wake recovery behind the disks and the effect of flow acceleration around the disks. The experiment was completed in the Chilworth Flume at the University of Southampton. The fume was 1.25 m wide and 0.3 m deep. Each of the three disks had a diameter of 0.1 m, a thickness of 0.01 m, and a porosity of 0.48. The first two disks were placed in the center of the channel with a 0.25 m, or 2.5 disk diameter, lateral spacing between the centerline of the two disks. The third disk was placed in the middle of the flume 0.3 m downstream of the first two disks. The velocity profiles through the width of the flume were measured at 5, 7, 9, and 25 device diameters downstream of the first two disks. The inlet velocity profile was not uniform, but was recorded and had an average velocity of 0.26 ms^{-1}. The experiments showed distinct wakes behind each disk with a substantial decrease in velocity. The individual wakes merged between 7-9 device diameters downstream and the velocity field was mostly recovered by 20 device diameters.

Experiments using single disk and two disk arrays were used to determine the coefficient of thrust of the porous disk. These disks were of the same size, geometry and porosity as the three-disk experiment. These experiments were also done in the same flume with nearly similar inflow conditions. The thrust load on the disk was recorded and used to determine a coefficient of thrust. The coefficient of thrust for the single and two disks arrays were found using actuator disk theory, equation 3.5, and ranged from 0.91 to 1.08. (Myers and Bahaj 2011). The higher coefficient of thrust values correlate with closer lateral device spacing.

Numerical Models

A numerical model of the three porous-disk array experiment was created in the CFD software package Star-CCM+®. The purpose of this model was to optimize the SA turbulence diffusivity and to verify mesh quality. The dimensions of the Chilworth flume were used to create the domain. No-slip wall boundary conditions were used to mimic the bottom and sides of the flume. The top surface was modeled first as a symmetric boundary layer and then as a free-surface. The inlet boundary condition was set as a velocity inlet using the recorded experimental inflow velocities. The outlet pressure was referenced to zero gauge at standard atmospheric conditions. The simulation was solved as a steady state problem and then verified against transient simulation. Velocities were recorded at 5, 7, 9, and 25 disk diameters downstream from the front two disks. These velocity profiles were then used to calibrate the SA diffusivity to get a near matching wake recovery.

The first part of the calibration was determining an optimum mesh size. An optimum mesh size refers to the smallest number of elements in a mesh required for the solution to no longer be affected by mesh size. The number of elements within a mesh is directly related to computational time and volatile memory, or RAM, usage. The higher the element count the longer it takes the simulation to solve and the higher the memory cost. The CFD program used has a wide range of built-in options for meshing control. The program allows the use of polyhedral or tetrahedral cells to mesh a 3-D fluid domain. Either one of these cell types could have been used; however there are some advantages in using the polyhedral cells. The polyhedral mesh uses approximately five times fewer elements than the tetrahedral equivalent, therefore requiring much less computing memory and power, and provides the same level of accuracy (CD-Adapco). Star-CCM+® controls the mesh size by specifying a base size for cells, polyhedral core density, and surface growth rates. The program also allows for mesh refinements along surfaces and boundaries and the use of volumetric controls. Volumetric controls are used to specify a particular volume within a domain that can be refined using newly defined mesh parameters. This is useful for refining the mesh around the disks and over the wake. The refinement around the disks was a rectangular volume that began three device diameters upstream and three device diameters downstream, compete depth of the flume, and two device diameters out from either side of the disks towards the walls. The wake profile utilized the same depth and lateral dimensions as the disk volumetric control, but began downstream of the disks and continued to the extent of the domain. The last refinement was at the interface between the disks and the rest of the domain. These refinements allowed for a smooth transition between inflow, porous disks, and the wake. The volumetric controls used in the calibration simulation can be seen in Figure 5.1. The simulation was meshed in an iterative process starting from a really refined mesh to a course mesh until the velocity profile at 5D, 7D, and 25D across tests no longer converged. The last mesh with the converged velocity profile was used. The most refined mesh started with approximately 4.5 million cells and the optimally refined mesh size was approximately 350 thousand cells. The diffusivity value specified for the SA turbulence model was left at the program default of $1e^{-5}$ m^2s^{-1} until the mesh optimization was complete.

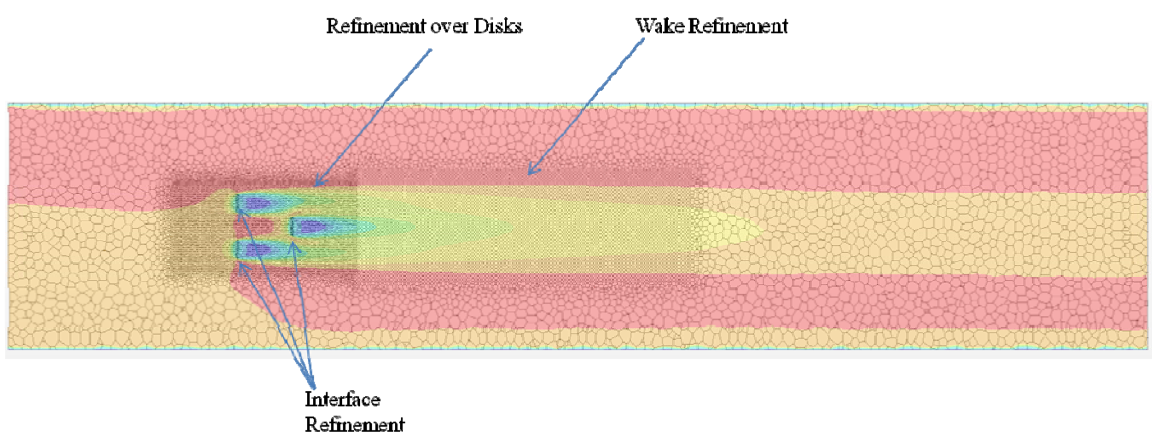

Figure 5.1: Three porous disk cross-sectional overhead view

A volume-of-fluid (VOF) model was also used to determine if there were any adverse effects due to pressure release at the air-water interface. The steady state solution never converged on a result for the VOF method, so an implicit unsteady solution form was used. The implicit unsteady VOF simulation showed little deviation in surface height at the air-water interface. Figure 5.2 shows the air-water interface through a centralized vertical slice of the domain. The velocities at 5, 7, 9, 25 disk diameters downstream correlated with the steady state simulations quite well. The symmetry-plane was used for the top boundary for the remainder of calibration.

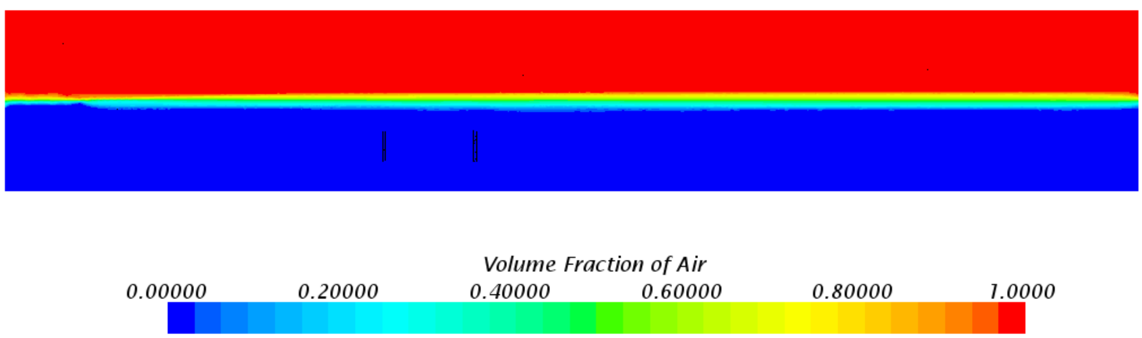

Figure 5.2: Three porous disk VOF air water interface

Once the mesh size and the top boundary were established, the physical parameters of the problem were calibrated. The diffusivities were tested from 1.0e-6 to 1.0, and it was found that a diffusivity of $1.25e^{-4}$ m^2s^{-1} most accurately fit the experimental data. The porosity of disks matched experimental value of 0.48, and the inertial/viscous losses through each porous disk were calculated to be $8.22e^5$ kgm^{-4} and $3.26e^3$ $kgm^{-3}s^{-1}$, respectively. Figure 5.3 shows the horizontal velocity profile at the mid-plane of the disks and Figure 5.4 shows the wake velocity comparison between the Chilworth flume experiment and the numerical simulation at the recorded distances downstream. There is good agreement between the experimental and the numerical simulation.

The last simulation for the calibration was of the flume with one porous disk. This simulation used all of the mesh parameters and physical characteristics calibrated above. The purpose of this simulation was to confirm the accuracy of the thrust loading on the disks. Myers and Bahaj reported that the coefficient of thrust on a single porous disk was 0.91 to 1.08. The coefficient of thrust found within the single disk simulation was 0.98 which is around 8% error of the experimental value. This calculation used the average inflow of 0.26ms^{-1} for the inflow velocity for equation 3.5.

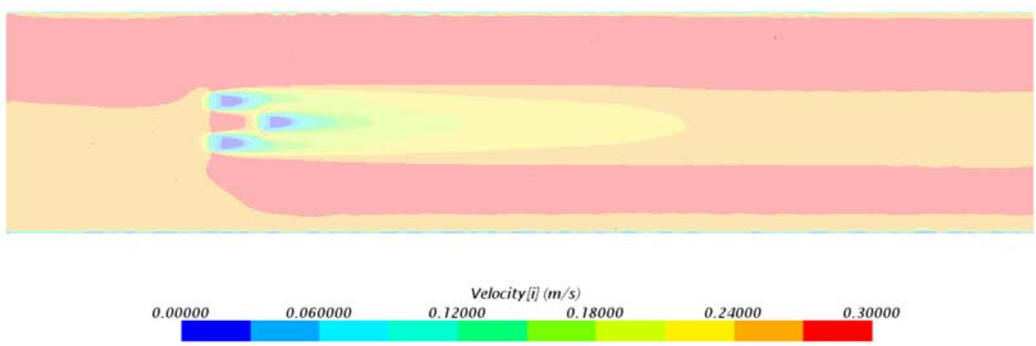

Figure 5.3: Three porous disk velocity profile through the central cross-section

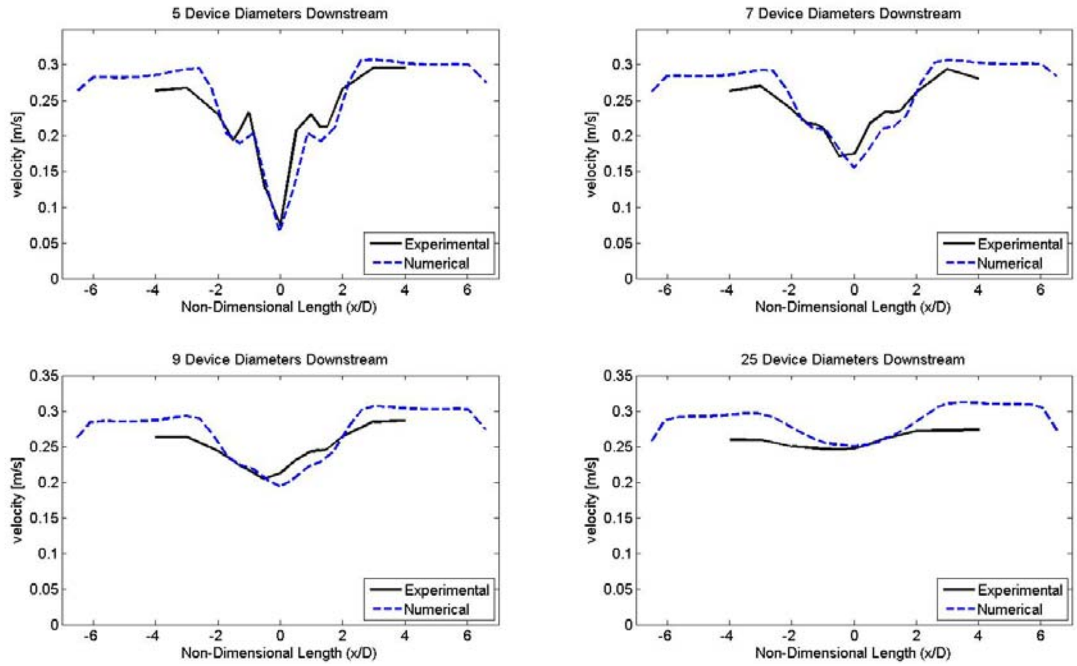

Figure 5.4: Three porous disk downstream velocity comparison, (Myers and Bahaj 2011)

Array Simulations

The numerical models used to evaluate array performance were built off the calibrated 3-disk model. The physical parameters of the calibration simulation including diffusivity and porosity were applied to the array simulations across each bathymetry. However, gravity was not included in the simulations, as performance based on depth was not evaluated. The inlet velocity for the array simulations was set to $0.25ms^{-1}$, as this value was close to the average inflow velocity used in the calibration model. The mesh properties for the domain base size, interface refinement, and each volumetric control were used as a basis for meshing the larger array domains. An initial simulation was performed using the (15D/4D) array to determine the required distances from the array to the boundaries, so that the array experienced no effects from the boundaries. Once the size of the domain was established twenty simulations were constructed using the different arrays layouts. The mesh cell count between simulations differed because the lateral and longitudinal length of the volumetric controls changed dependent upon array spacing. Each simulation used the same forms of volumetric control: a rectangle around the wake, and a rectangle around the disks. For the arrays with 3D and 4D lateral spacing, volumetric controls were applied in the form of 9 rectangles each one enveloping a column of disks.

ARRAYS WITHIN AN OPEN CHANNEL

The purpose of this thesis was to explore the effect of bathymetry on array performance and characteristics. In order to understand the effects of bed bathymetry on array performance, there must be a baseline understanding of array performance in an unconstrained environment. Bathymetry 0 was created to formulate a baseline for characteristic properties for each array layout used in the bathymetric case study. Bathymetry 0, or the open channel bathymetry, was created so that there were no outside forces or boundary conditions affecting the flow around the array of porous disks. Twenty linear arrays were tested in Bathymetry 0. Every combination of a lateral spacing of 1.25D, 2D, 3D, 4D and longitudinal spacing of 2D, 3D, 5D, 7D, 11D, and 15D were tested. Each simulation used a uniform inflow velocity of $0.25ms^{-1}$ and a 0 gauge pressure release at the end of the domain. The main characteristics of interest are the thrust loads on the disks and the wake profile after the arrays. The actuator disk model can be used to relate the thrust loads to a coefficient of power, which turbine developers can use as a quick mechanism to evaluate performance. The thrust loads were recorded for each disk within every array and the total thrust load for an array was calculated by summing all the thrust loads per disk. The total thrust loads were plotted against the non-dimensional longitudinal spacing in terms of disk diameter (D). This created reference curves for performance based on array spacing for an open channel. These curves were used as a baseline for comparison against the four bathymetric cases. The fluid velocities were recorded through the center of the array to the end of the domain to characterize the flow through an array and wake recovery. The downstream/longitudinal distance was also non-dimensionalized in terms of disk diameters.

Force output increased in Bathymetry 0 as the longitudinal spacing between the disks increased until approximately 15D, as seen in Figure 6.1. This behavior has been characterized before and is expected due to the velocity deficit behind each disk. As the spacing is increased the wake velocity after each disk is able to further recover, thus providing higher thrust loads on the next disk. Recall that power is directly related to velocity cubed and thrust loads are related to velocity squared. The higher the velocity recovery the higher the possible power generation. This trend will continue until the spacing is great enough that each disk operates as if it were independent of the array. Increasing the spacing past this point will not increase performance as the flow velocity will never reach the inlet velocity without external forces. Figure 6.2 shows this effect through velocity recovery using the (3D/3D), (7D/3D), and (11D/3D) arrays. The velocity recovery is evaluated in non-dimensional velocity deficit and the longitudinal length is reported in disk diameters. The velocity deficit is defined by one minus the velocity of interest over the inflow velocity. Each plot starts at the front row of the array and continues until the end of the domain. A velocity deficit of one indicates that flow has stopped and zero indicates that the flow has fully recovered. The velocity after each disk on the (3D/3D) does not recover to a consistent value, because there is not enough longitudinal space between the rows. On the other hand, the (7D/3D) array disks are spaced far enough apart, longitudinally, that the velocity after each disk is able to recover to the same value. The (11D/3D) array has larger longitudinal spacing than the (7D/3D) array so the velocities after the disks are able to recover further still.

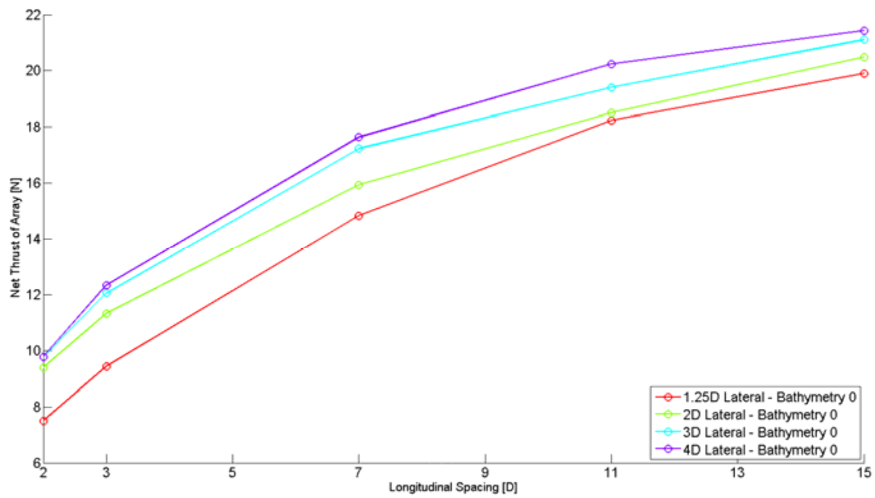

Figure 6.1: Total thrust loads on arrays in Bathymetry 0

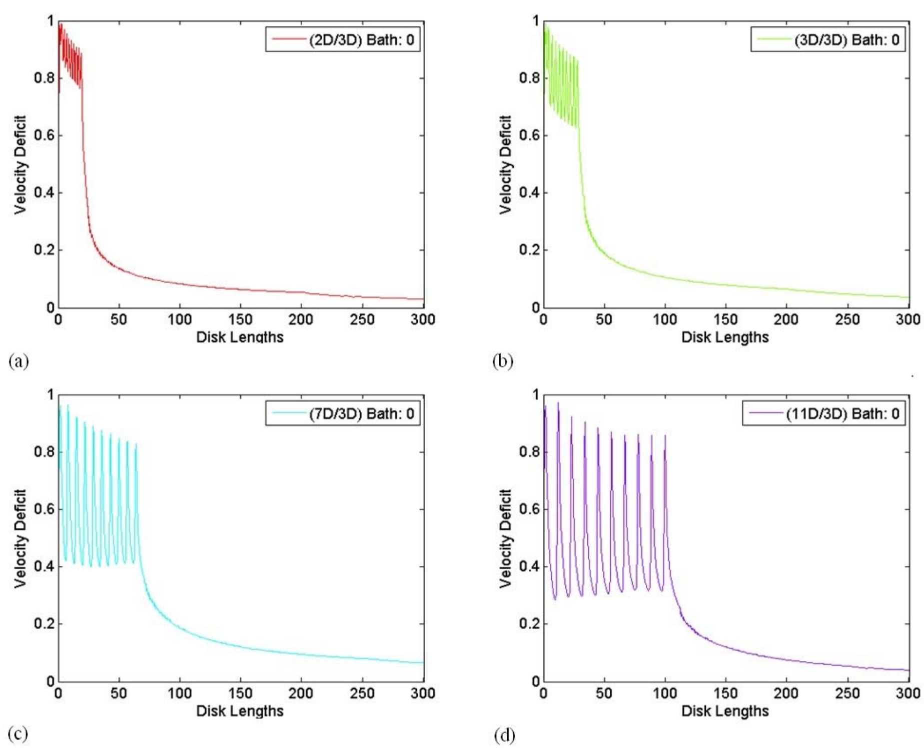

Figure 6.2: Velocity profiles by longitudinal spacing for Bathymetry 0 (a) (2D/3D), (b) (3D/3D), (c) (7D/3D), (d) (11D/3D)

The effect of altering the lateral spacing on performance was relatively small in comparison, but an increased spacing produced larger thrust loads. Diminishing returns for lateral spacing occurred after three disk diameter spacing as seen in comparing Figures 6.3 (c) and (d). Figure 6.3 specifically shows lateral spacing for the 7D longitudinal spacing cases; however, the trend held true for all the longitudinal spacing. The lateral spacing case of 1.25D was tested in an attempt to assess the flow acceleration principle seen in the three disk calibration case. Unlike the calibration case, it appears that the disks were too close and flow no longer accelerated between them causing a decrease in performance. Figure 6.4 shows the cross-sectional velocity profile at row 1 for the (7D/1.25D) array and Figure 6.5 shows the cross-sectional velocity profile at row 10 for the (7D/1.25D) array. Figure 6.6 shows the cross-sectional velocity profile at row 1 for the (7D/3D) longitude spacing and Figure 6.7 shows the cross-sectional velocity profile at row 10 for the (7D/3D) array. Row 1 and row 10 were chosen to display the extremes of the velocity profiles around the disks. Over the rows of the (7D/3D) array it is clear that flow is accelerating uniformly around each disk as seen in Figures 6.6 and 6.7. Due to the close proximity of the disks in the (7D/1.25D) array the acceleration of flow around each disk is not uniform as seen in Figures 6.4 and 6.5. The reason is similar to the longitudinal spacing as there needs to be enough space for the flow to develop around each individual disk and once a certain distance is reached any further increase in spacing will not provide any additional benefit.

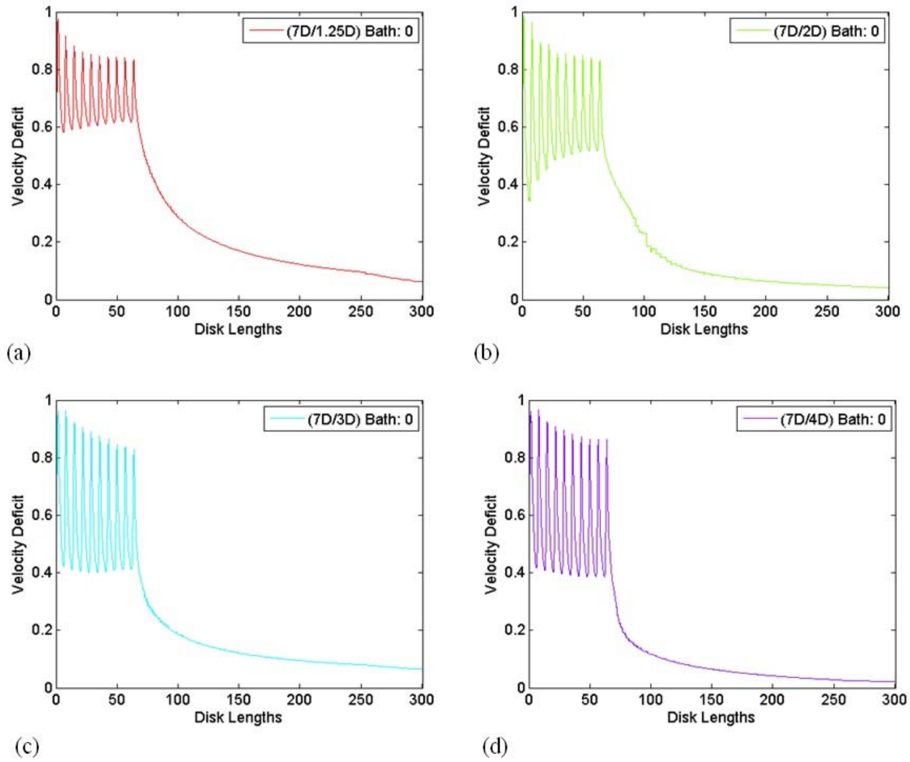

Figure 6.3: Velocity profiles by lateral spacing for Bathymetry 0 (a) (7D/1.25D), (b) (7D/3D), (c) (7D/2D), (d) (7D/4D)

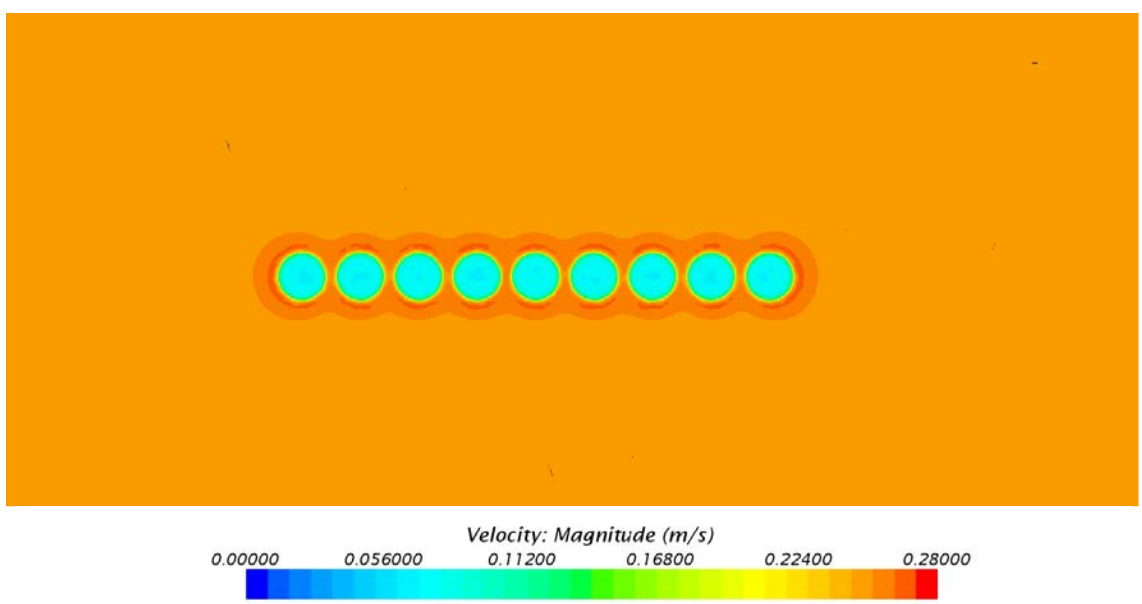

Figure 6.4: Row 1 of the (7D/1.25D) array for Bathymetry 0

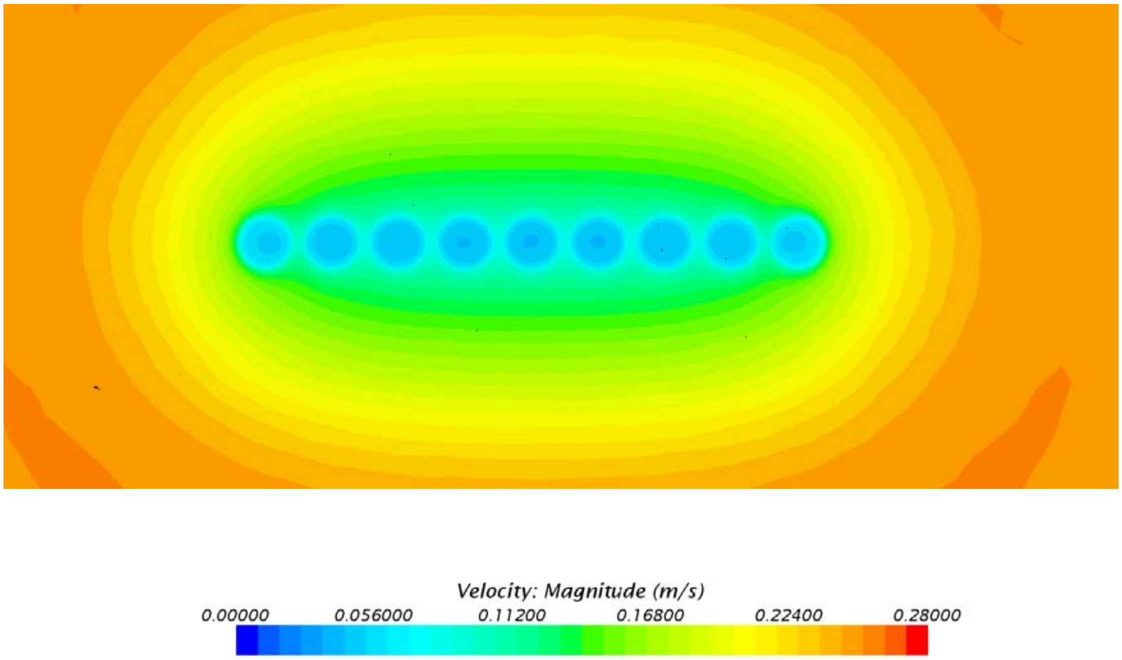

Figure 6.5: Row 10 of the (7D/1.25D) array for Bathymetry

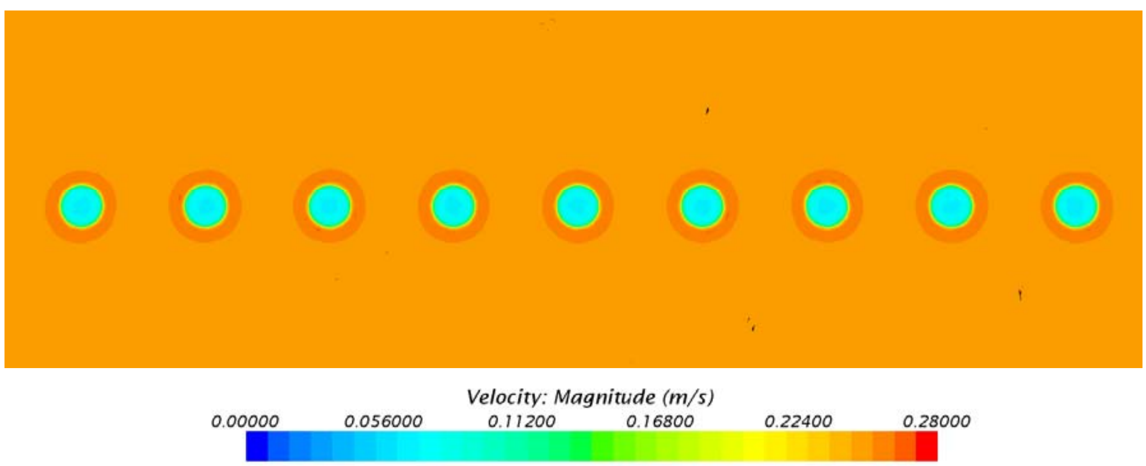

Figure 6.6: Row 1 of the (7D/3D) array for Bathymetry 0

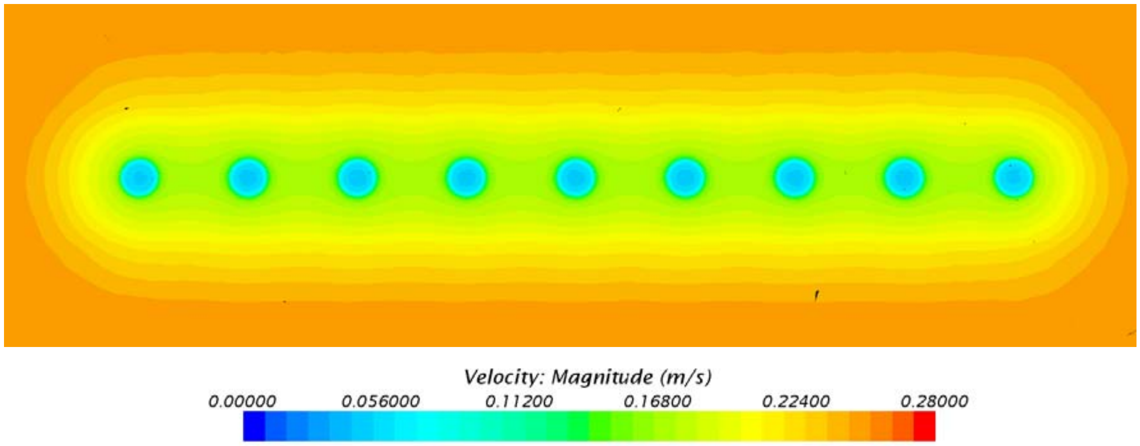

Figure 6.7: Row 10 of the (7D/3D) array for Bathymetry 0

The overall thrust loads on the arrays follow the predicted pattern for longitudinal and lateral spacing. However, if each individual row within an arrays is considered there is an unexpected trend in thrust. General thought suggest that as flow moves through an array, energy is extracted by each disk causing the flow to slow after each subsequent row resulting in decreased loading. This trend does not appear to hold for these simulations. Figure 6.8 shows the thrust load by row for each of those simulations and Figure 6.9 shows the thrust loads on each individual disk by row. After the first row there is a large drop in thrust as expected; however, after the second row the thrust loads increased per row. This trend is present across all of the array configurations of Bathymetry 0. This type of performance gain for later rows has been observed before (Churchfield et. all. 2012). In the paper “A Large-Eddy Simulation of Wind-Plane Aerodynamics” the increase in power production for the later rows was thought to be from an “increased wake meandering of the more downstream wakes” (Churchfield et. all. 2012). In this model there is no wake meandering, because there is no rotational motion from the porous disks. The increase in thrust loads throughout the array may be attributed to an increasing downstream pressure deficit within the array and reduced resistance after the final row of devices. All the lateral spaced arrays resulted in similar results so the 3D lateral spaced arrays and are used for the longitudinal comparisons. Figure 6.9 shows the thrust loads by disk in each row for each of the 3D lateral spaced arrays. In the (3D/3D) array the thrust of rows 2 through 10 were within 30% of each other and rows 2 through 10 were within 25% for the (7D/3D) array. The (7D/3D) array has a narrower spread for thrust loads over each row than the (3D/3D) case, as seen in Figure 6.9 (c). This is because the (7D/3D) has a larger longitudinal spacing than the (3D/3D) which allows the velocity to recover further and converge to the same value each time. Figure 6.9 (d) shows the thrust loads on the (11D/3D) array. The flow in the (11D/3D) has more downstream distance to recover than the (7D/3D) array, so the thrust loads for rows 2 through 10 vary even less than the in (7D/3D) array.

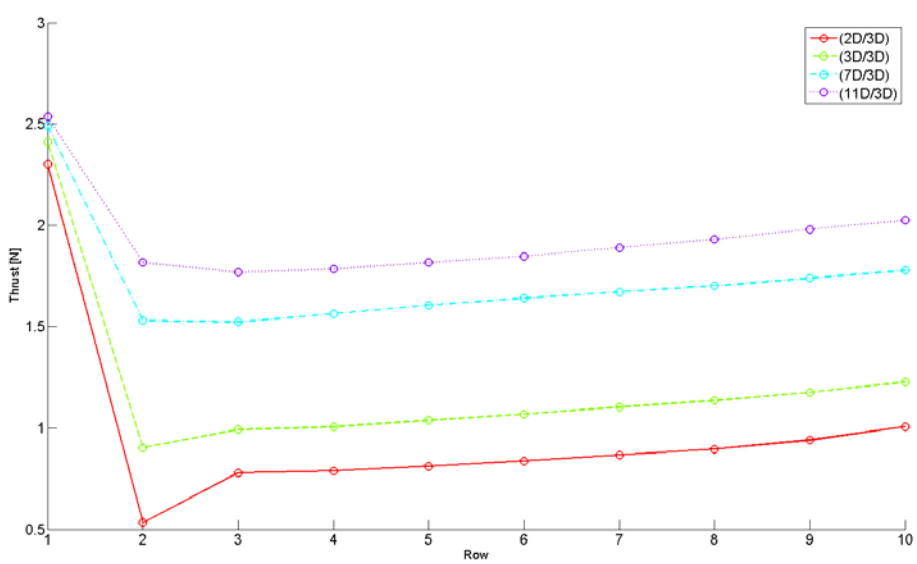

Figure 6.8: Thrust loads on rows for Bathymetry 0

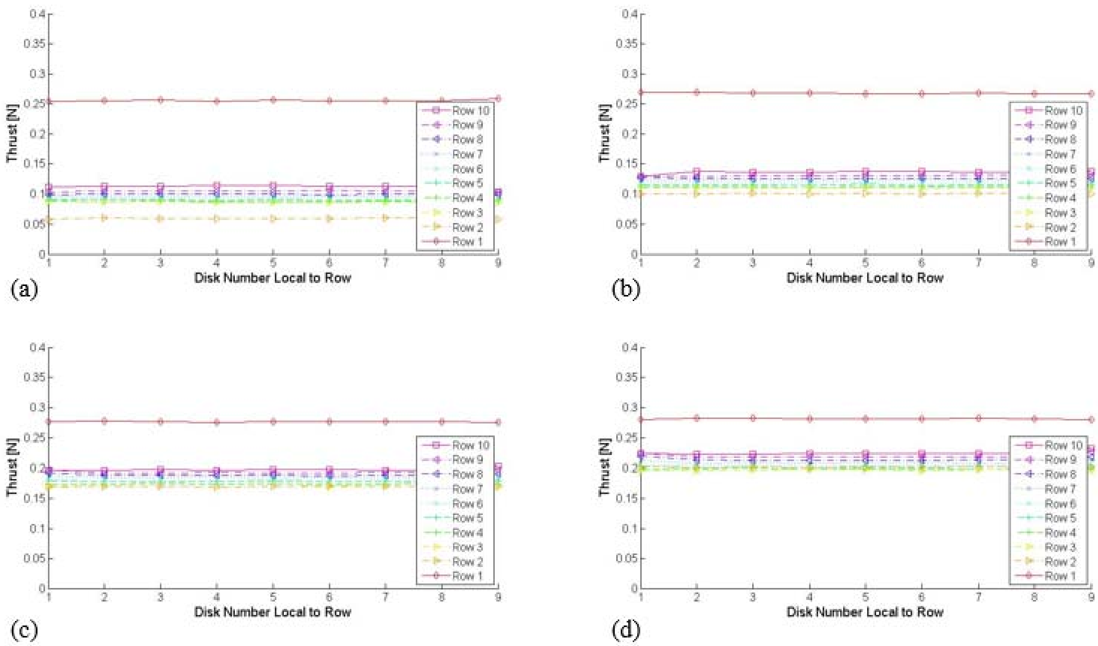

Figure 6.9: Thrust loads on disks by row for Bathymetry 0 (a) (2D/3D), (b) (3D/3D), (c) (7D/3D), (d) (11D/3D)

It is often more beneficial to view performance of marine hydrokinetic turbines in terms of their non-dimensional coefficient of power. Thrust loads and velocities will be specific to the site and inflow conditions. Equation 3.2 can be used to relate the coefficient of power to dimensional power through velocity or the axial induction factor. Once either of those terms are known then the performance of the turbine can be evaluated for any system. In the case of the arrays each array can also be evaluated for its own coefficients of thrust and power, as seen in Figure 6.10. Equation 3.5 was used to obtain a coefficient of thrusts from the total thrust loads and the upstream velocity of Bathymetry 0. The upstream velocity is the inlet velocity which is at $0.25ms^{-1}$ and the area is in terms of the total disk area or the area of one disk multiplied by the number of rows and columns. Equation 3.5 can also be used calculate the axial induction factor from the coefficient of thrust. The axial induction factor then can be applied to equation 3.3 to determine a coefficient of power for the array. Naturally the coefficient of thrust curves follows the same trend as the total thrust loads plot; however, the coefficient of power curves is slightly different. After approximately 7D downstream the array starts approaching the Betz limit which is the theoretical performance maximum. The thrust load plots can be deceiving, as the thrust loads can increase, but the total power output can remain the same. From a developer standpoint the most optimal spacing for this particular “device” and operation condition would be the (7D/3D) array.

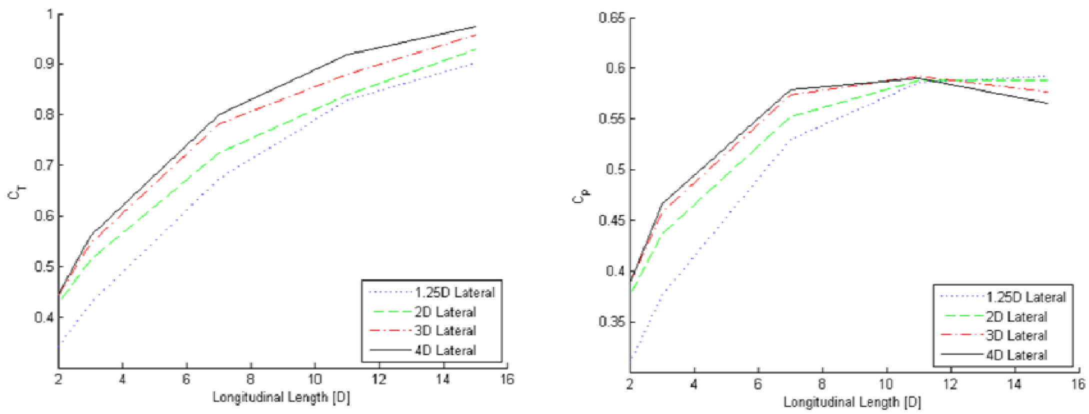

(a) (b)

Figure 6.10: Coefficients of thrust and power for Bathymetry 0, (a) thrust, (b) power

Another key metric that MHK developers are concerned about are the wake recovery profiles of the arrays. The wake profile is used to categorize how long it takes the flow to return to normal and principally determines the performance and loads of devices located downstream of others in the array. Additionally, the effects of arrays on marine life, sediment transport, and other water quality metrics is still relatively unknown, so a faster recovery could limit adverse effects. It may also be necessary to deploy multiple arrays within semi-close proximities, where the downstream array deployment will rely on the wake from the upstream array, similar to individual devices within an array. It is important to know how far to space these arrays to operate efficiently. In this thesis wake recovery is in terms of velocity deficit. The wake recovery is recorded from the last row of an array to the end of the domain. The distance downstream is in terms of non-dimensional length (distance / device diameter). Figure 6.11 shows the wake recovery for each array organized by longitudinal spacing and Figure 6.12 shows the wake recovery for each array organized by lateral spacing. Each array had a similar velocity recovery profile, but the wake recovery did not appear to have a consistent pattern based on longitudinal spacing. It was clear that the lateral spacing of 1.25D had the slowest wake recovery; however, there was no distinct relationship for the other lateral spacing. Within the first 50 - 100 device lengths most of the arrays recovered between 80% and 90% of the inlet velocity. The arrays reached a maximum recovery between 200 - 250 device lengths. The arrays tested had longitudinal lengths between 20 and 150 device lengths. The recovery lengths were between 1.67 and 10 array lengths; which indicates that longitudinal spacing does not correlate strongly to wake recovery. It may be possible to characterize array recovery based number of devices alone as there is no clear relation to wake recovery and device spacing; however, this was not tested.

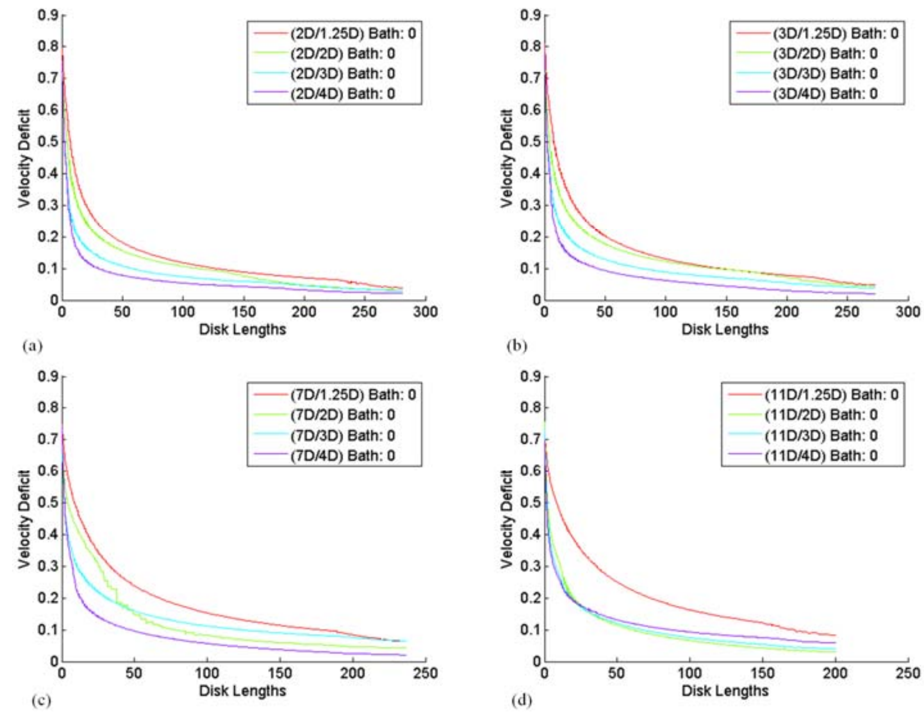

Figure 6.11: Wake recovery by lateral spacing for Bathymetry 0, (a) (2D/XD), (b) 3D/XD), (c) (7D/XD), (d) (11D/XD)

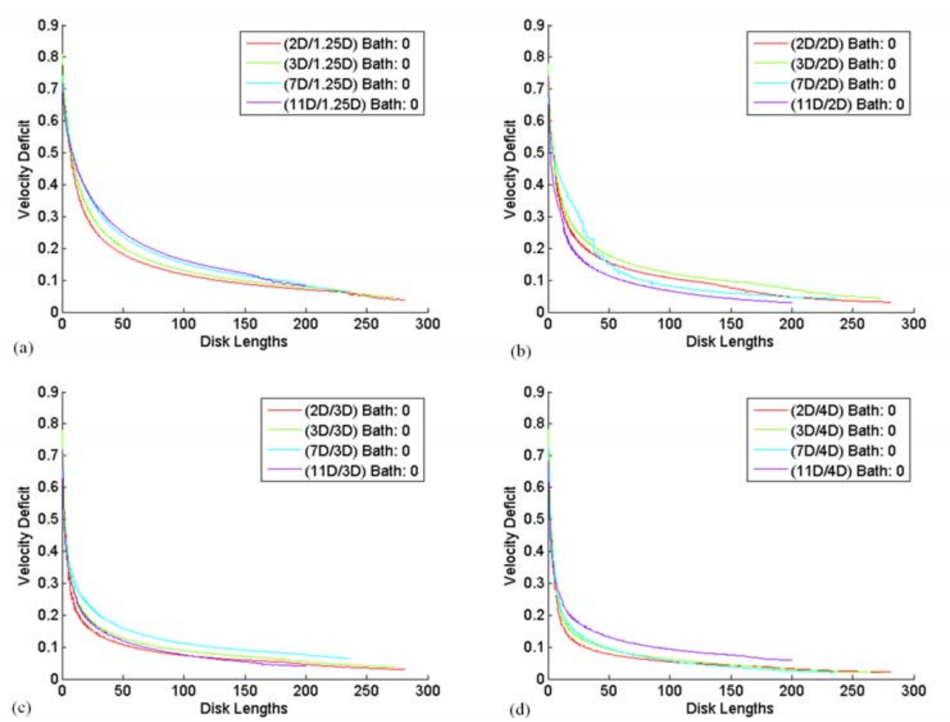

Figure 6.12: Wake recovery by longitudinal spacing for Bathymetry 0, (a) 1.25D, (b) 2D, (c) 3D, (d) 4D

This chapter discussed the baseline data established for arrays in an open channel. The thrust loads on the disks were analyzed to determine the performance of the arrays. The thrust loads were used as a surrogate for power using actuator disk theory. The thrust loads were used to calculate an axial induction factor for each array as a whole. The coefficient of power for each array was then calculated using the axial induction factor. The total thrust loads on the arrays increased as the longitudinal and lateral spacing increased; however, the power reached a relative maximum after 7 longitudinal device diameters. The maximum power occurs at the Betz limit when the axial induction factor is 1/3. Once the axial induction factor has increased past 1/3, the loading has increased on the disks, but the potential power generation remains the same. The axial induction factor of 1/3 relates to a coefficient of thrust of approximately 0.9. Any array with a coefficient of thrust over 0.9 has a higher loading condition, but is not generating any additional power. The 11D and 15D longitudinal spaced arrays are examples of arrays that are operating at this condition. This condition may be attributed to the porous specifications applied to these disks, which is likely operating outside of its peak performance window.

The velocity profile through the arrays to the end of the domain were also quantified to characterize the flow through an array and the wake recovery. The flow velocity between rows of devices was dependent on row spacing. The larger the spacing the larger the velocity recovery between rows. However, the wake after the arrays was not affected by the device spacing. The wake after each array followed the same profile converging between 200 and 250 device diameters. If multiple arrays were deployed, the downstream array would need to be placed approximately 250 device diameters away to remain independent.

ARRAYS OVER SLOPED BATHYMETRIES

The bathymetry of a system has the potential to change the performance characteristics of an array. The same analyses that were performed for the reference bathymetry were applied to each bathymetric case. This study evaluates that change by comparing the thrust loads and wake recovery of the open channel bathymetry to the two cases with bottom bathymetry. The flow field of the domain is expected to change due to the new topography; however, the question remains as to how this change in flow field effects the array performance and wake recovery. Do the performance curves of Bathymetry 0 just shift up/down, become slightly different, or do the curves become completely different? If the curves uniformly shift in magnitude then bathymetry does not necessarily need to be taken into account for general array performance evaluation. The uniform shift would indicate that each array will have the same relative performance to each other array based on lateral and longitudinal spacing. If there is only a slight change it may be possible to still use an open channel as a first approximation of device layout. If the performance curve drastically changes, then the open channel bathymetric case cannot not be used, even as a first step to predict array performance. Developers would have to test each array layout over the new bathymetry to determine the optimal layout.

Bathymetry A

The purpose of the bathymetry A was to provide a bottom bathymetry that varied across the lateral spacing of the arrays. This type of topography can be related to locations that are off the cost and close-to-shore, where an array is aligned parallel to the coastline. Twenty of the arrays that were tested in Bathymetry 0 were relocated over Bathymetry A. Every combination of a lateral spacing of 1.25D, 2D, 3D, 4D and longitudinal spacing of 2D, 3D, 5D, 7D, 11D were tested. Like Bathymetry 0 the main characteristics of interest are the thrust loads, pressure profile through the array, and the wake profile after the array.

Force output increased in Bathymetry A as the longitudinal spacing between the disks increased, as seen in Figure 7.1. This behavior is identical to what was seen in the reference bathymetry. As spacing is increased, the more the velocity is able to recover; which results in higher velocities, and therefore thrust loads, on the downstream rows of disks. This trend will continue until the spacing is large enough that each disk operates as if it were independent of the array, at which point increasing the spacing will not increase performance.

Figure 7.2 shows the velocity recovery using the (3D/3D), (7D/3D), and (11D/3D) arrays. Like Bathymetry 0, the velocity recovery was evaluated in non-dimensional velocity deficit and the longitudinal length was reported in disk diameters. Each plot starts at the front row of the array and continues until the end of the domain. Similar to Bathymetry 0 the velocity after each disk on the (3D/3D) array does not have enough space to recover before experiencing the proceeding disks and the (7D/3D) array are spaced far enough apart longitudinally that the velocity after each disk is able to recover to the same point. The (11D/3D) array has larger longitudinal spacing so the velocity is able to recover even further.

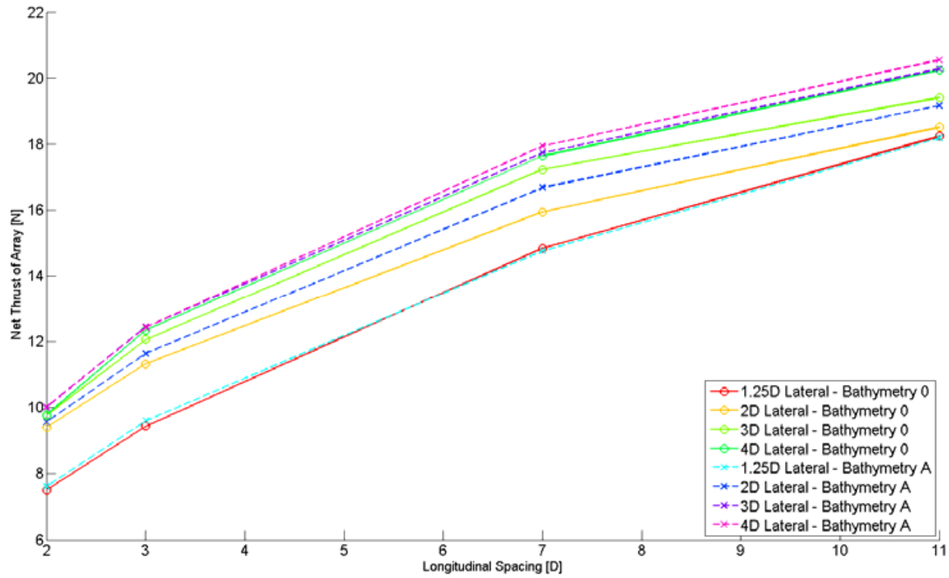

Figure 7.1: Total thrust loads on arrays in Bathymetry A

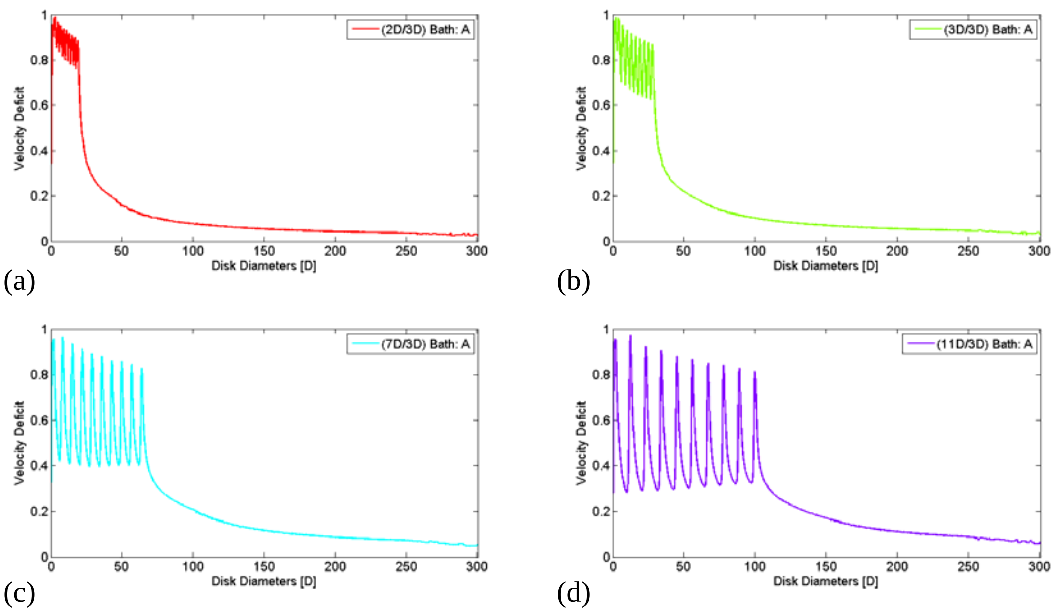

Figure 7.2: Velocity Profiles by Longitudinal Spacing for Bathymetry A, (a) (2D/3D), (b) (3D/3D), (c) (7D/3D), (d) (11D/3D)

Similar to the reference bathymetry the effect of altering the lateral spacing on performance was relatively small in comparison to the lateral spacing. The larger the lateral spacing the larger thrust load until approximately 3 device diameters; at which point diminishing returns occur. Even with the laterally sloping bed, the 1.25D lateral spacing was still close enough that flow did not accelerate between the disks and instead moved around the sides of the array. The overall thrust loads on the arrays followed the same pattern as Bathymetry 0 for longitudinal and lateral spacing. The first rows experienced the highest loading followed by a sudden drop in loading for the second row and increased loading for each additional row. Figure 7.3 shows the thrust loads on each row for arrays with 3D lateral spacing. The cause of this is still likely due to an increasing, downstream pressure deficit within the array and reduced resistance after the final row of devices. This trend is present across all of the array configurations of Bathymetry A. As with Bathymetry 0, the variation of thrust loads from row 2 through 10 is relatively small with the exception of the 2D longitudinal spacing which has a 60% thrust load range. The (3D/3D) has a thrust load variance for rows 2 through 10 of 33%. Similar to before the (7D/3D) has a thrust variance for rows 2 through 10 of 23% and the (11D/3D) array is within 15%.

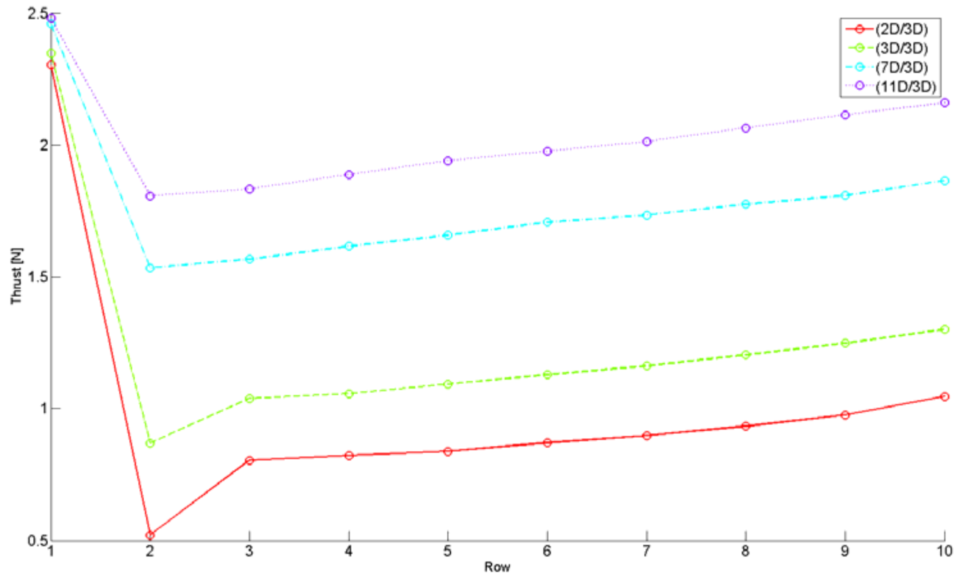

Figure 7.3: Thrust loads by rows for Bathymetry A

The coefficient of thrust and power for the arrays were also similar to what was found in the open reference channel, and can be seen in Figure 7.4. As before, the coefficient of thrust curves mirror the total thrust loads curves in Figure 7.1, with Figure 7.5 showing a comparison of the thrust and power coefficients for Bathymetry 0 with the 3D lateral array spacing. The curves are nearly identical between the open channel and over the lateral sloped bottom. This relationship suggests that array optimizations within an open channel could be applied to arrays in currents that run parallel to a coast or shoreline.

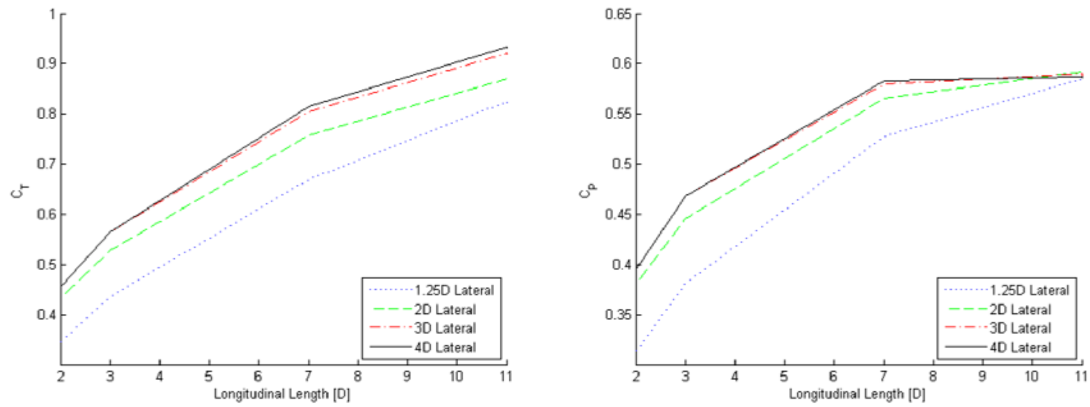

(a) (b)

Figure 7.4: Coefficients of thrust and power for Bathymetry A, (a) thrust, (b) power

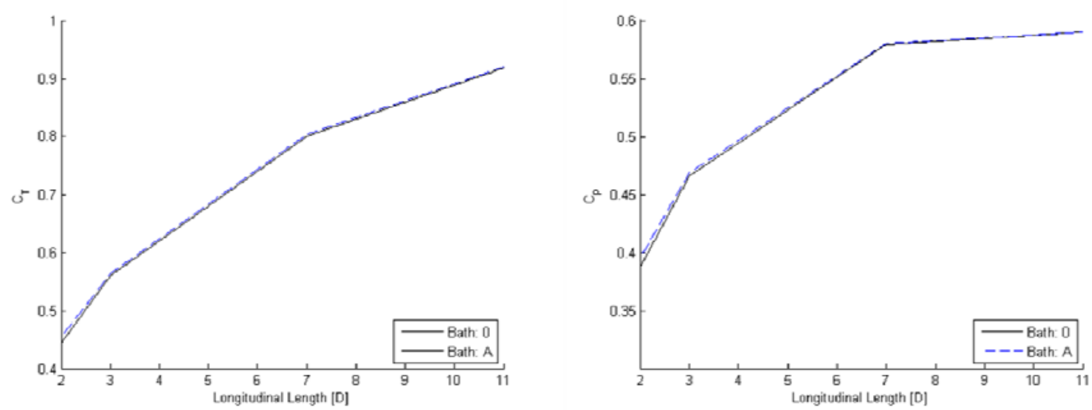

(a) (b)

Figure 7.5: Coefficient comparisons of Bathymetry 0 and A for 3D lateral spacing, (a) coefficient of thrust, (b) coefficient of power

As expected then, the wake recovery of Bathymetry A is also similar to the reference channel. All of the wake recovery curves have similar profiles. The wake recovery is in terms of velocity deficit and was evaluated from the last row of an array to the end of the domain, non-dimensionalized by device diameters. Figure 7.6 shows the wake recovery for each array organized by longitudinal spacing and Figure 7.7 shows the wake recovery for each array organized by lateral spacing. Unlike the reference bathymetry it is clear that wake recovery is dependent upon lateral spacing. The larger the lateral spacing the faster the wake recovery. The longitudinal spacing has the opposite effect where the largest spacing recovers slowest and the smallest recovers first. Possibly counterintuitive, but the lateral spacing is a larger determining factor on wake recovery than downstream spacing of the disks. In general the wake recovery curves for a fixed lateral spacing are similar enough it could be possible to predict the wake recovery using any one of the arrays.

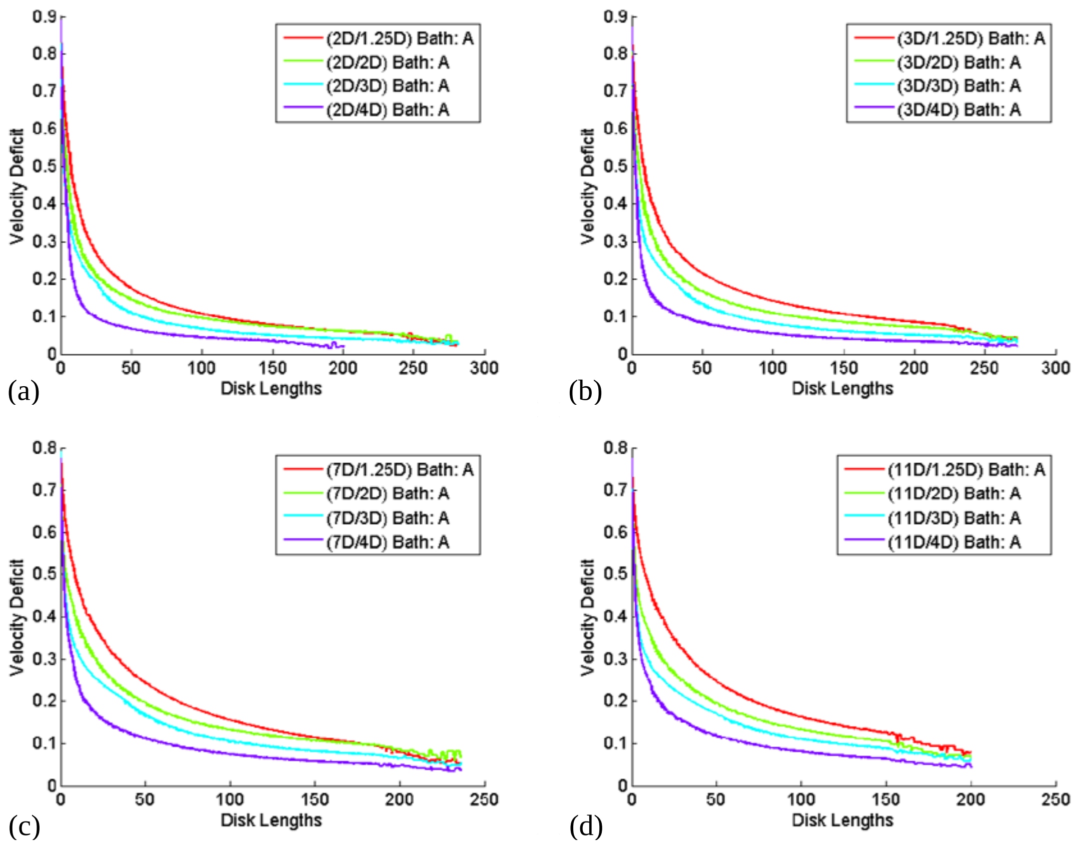

Figure 7.6: Wake recovery by longitudinal spacing for Bathymetry A (a) 1.25D, (b) 2D, (c) 3D, (d) 4D

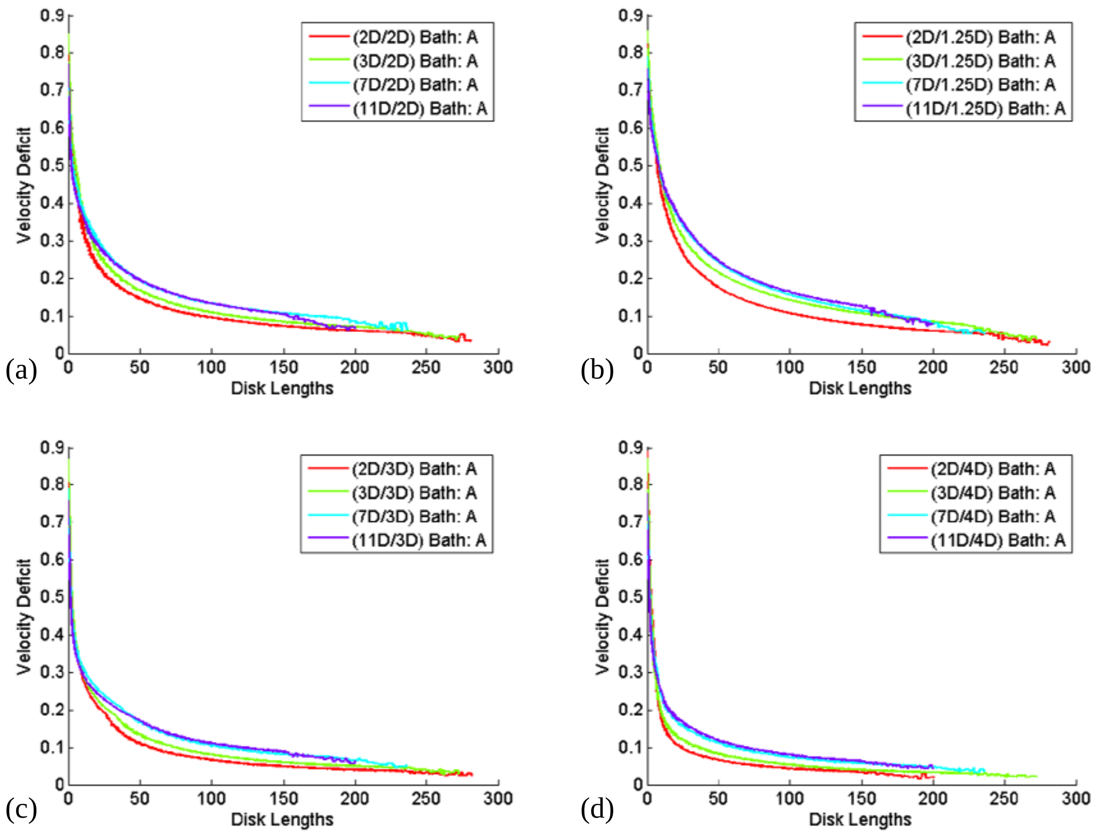

Figure 7.7: Wake recovery by lateral spacing for Bathymetry A. (a) 2D, (b) 1.25D, (c) 3D, (d) 4D

Bathymetry B

The purpose of Bathymetry B is to mimic a sloping bed in the direction of flow. This type of topography is often seen in riverine environments and tidal straits. The magnitude of the slope will vary from location to location; however, the slope used in Bathymetry B is larger than expected deployment sites in order to exemplify any changes. It is expected that similar bathymetries with shallower slopes will experience the same effects, but to a lesser degree. Additionally, “smaller,” local features, like sea-mounds, may induce a similar effect. Twenty arrays were used in the simulations of

Bathymetry B. Every combination of a lateral spacing of 1.25D, 2D, 3D, 4D and longitudinal spacing of 2D, 3D, 5D, 7D, 11D were simulated. Unlike the reference bathymetry and Bathymetry A, the longitudinal, or downstream location, over the bottom slope effects the performance of the arrays. Bathymetry B was split into two distinct scenarios, B1 and B2, in order to quantify the effects of longitudinal location of the array. In Bathymetry B1 the arrays are referenced such that the first row of the array remains at the start of the sloped bed, with succeeding rows locating into shallower waters as the spacing increases. In Bathymetry B2 the last row of the array is referenced to the apex of the sloped bed, with preceding rows increasing in distance from the bed as the longitudinal spacing increases.

Bathymetry B1

Force output increased in Bathymetry B1 as the longitudinal spacing between the disks increased, as seen in Figure 7.8. The manner of the increase is drastically different from the reference bathymetry. The thrust of the array increased by 70% from 3D to 7D longitudinal spacing; which is 27% higher than observed change in the reference bathymetry. All of these percent increases are much higher than Bathymetry 0, except for 2D to 3D longitudinal cases. This is due to the effect the sloping bottom has on the fluid flow. In fluid mechanics, conservations of mass can be used to relate the mass flow into a system, through the system and out of the system. Continuity is a function of density, ρ, time, t, and flow velocity, u as seen in equation 7.1. For steady state and incompressible flows, the volumetric flow rate into the system must be the same as the flow out of the system. Volumetric flow, Q, rate can be defined as the velocity of the fluid, u, multiplied by the cross-sectional area, A, it moves through, and because density is constant it can be removed from both sides of the equation. Equation 7.2 is continuity based on volumetric flow rate.

$$\frac{\partial \rho}{\partial t} + \nabla \cdot (\rho u) = 0 \tag{7.1}$$

$$A_1 u_1 = A_2 u_2 \tag{7.2}$$

As flow moves through the channel the cross-sectional area decreases. In order for conservation of mass to be satisfied, the velocity must increase downstream as seen in equation 7.2. It is this increase in velocity that increases the thrust loads on the disks. Recall that thrust is proportional to the velocity of the fluid squared. In the case of the 2D and 3D longitudinal spaced arrays, the longitudinal array lengths are not long enough for the decreased cross-sectional area to drastically affect flow velocities, so the thrust loads remain similar to Bathymetry 0.

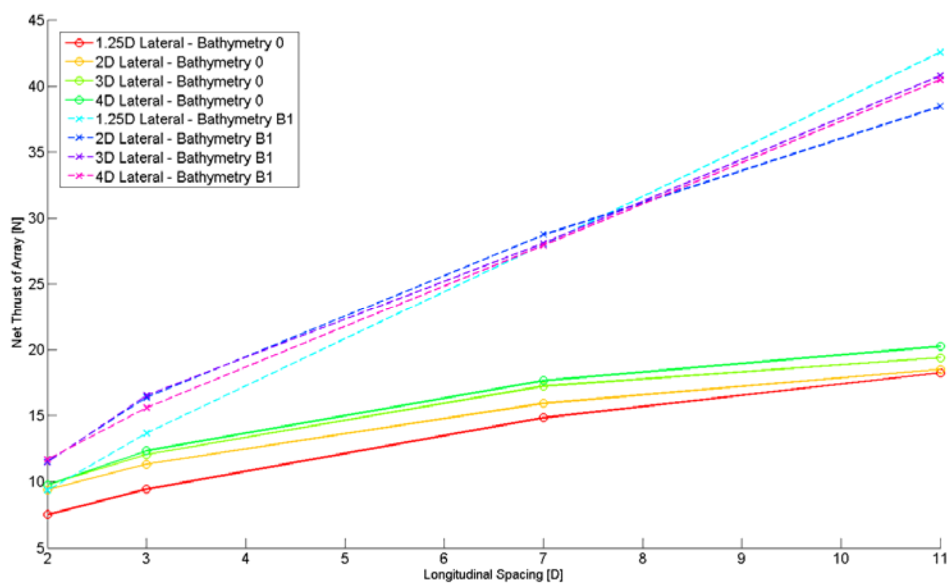

Figure 7.8: Total thrust loads for Bathymetries 0 and B1

There are now two competing effects taking place due to longitudinal spacing: wake recovery after the disks and increasing fluid velocity through continuity. As before, increasing the longitudinal spacing gives the velocity more time to recover and after some specific distance the velocity will have reached a max recovery point. The bathymetry of this system has altered this distance. The second effect on the longitudinal spacing is continuity. The longer the array is the smaller the cross-sectional area available for flow; which causes the velocity to increase even further than in the reference bathymetry case.

The profiles of the (2D/3D) and the (3D/3D) arrays, as seen in Figure 7.8, have similar profiles to those found in the reference study. Both of these arrays do not extend far over the sloped bed, so cross-sectional area change is minimal resulting in flow velocities through the array similar to Bathymetry 0. On the other hand, arrays (7D/3D) and (11D/3D) benefit from spacing and conservation of mass. In the reference bathymetry case both of these arrays encountered velocity deficits that converged after each disk. In the new bathymetry the velocity deficit continues to decrease due to the conservation of mass. Between the last two rows in the (7D/3D) array the velocity deficit was less than zero; which meant that the flow at the end of this section was actually greater than the inflow of the system. In the (11D/3D) array this happened over multiple rows.

Figure 7.9 shows the bathymetric effect on velocity recovery through the centerline of the array and the sloped section starts at zero and continues to 100 disk lengths. Unlike the longitudinal spacing the lateral spacing influence on performance was relatively small. The larger the lateral spacing the larger thrust load until approximately 3 device diameters; at which point diminishing returns occur. However, there is an exception. At 11D longitudinal spacing the 1.25D lateral spacing is able to outperform the 2D, 3D, and 4D spacing. This is possibly due to the sloping bottom forcing flow through subsequent rows of disks that would have otherwise been pathed around.

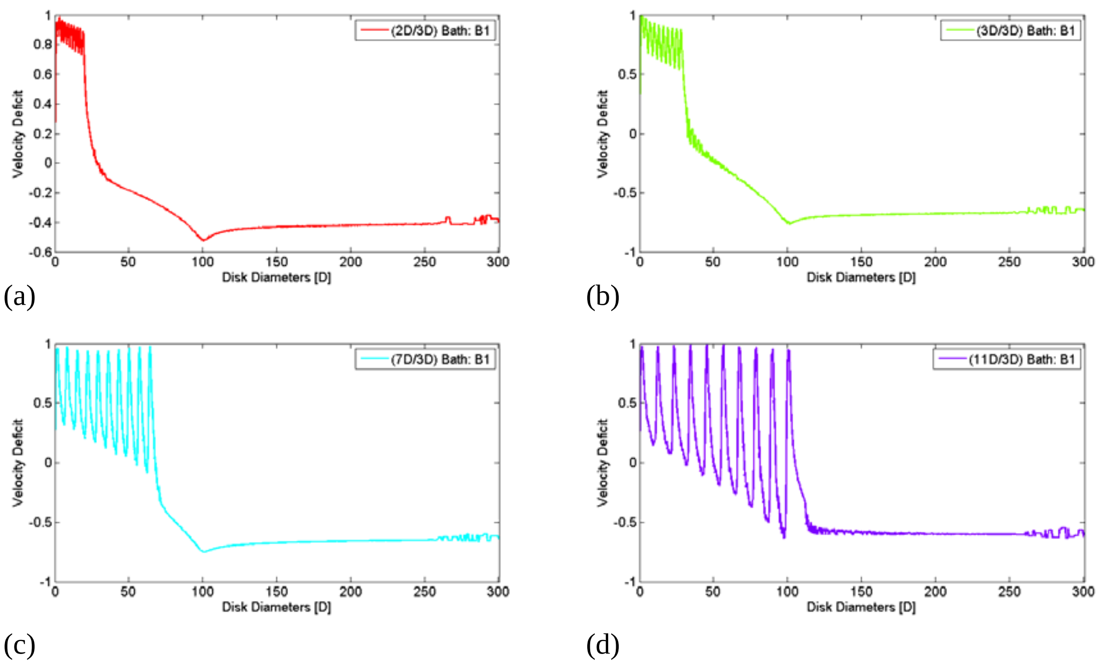

Figure 7.9: Velocity profiles by longitudinal spacing for Bathymetry B1 (a) (2D/3D), (b) (3D/3D), (c) (7D/3D), (d) (11D/3D)

The velocity deficit curves are directly related to the thrust loads on the disks. Figure 7.10 shows the thrust loads per row for four arrays within Bathymetry B1. The arrays with 2D and 3D longitudinal spacing have similar thrust loads to the reference bathymetry study. The first row experiences the largest loads, with the last three rows experiencing higher loads than the rows in the middle of the array. This pattern begins to break down once the longitudinal spacing is large enough that the reduction in area significantly increases the flow velocity. The 7D and 11D arrays extend over the majority of the sloped bed, so the arrays benefit from the larger longitudinal spacing in twos ways. First, as seen in Bathymetry 0, the flow velocity has more space to recover after each row. Second the arrays span over most of the sloped bed, so the decrease in cross-sectional area forces the flow to accelerate which in turn increases the thrust loads on the disks. The last three rows experience the highest thrust loads in Bathymetry B1. In Bathymetry 0 the spread in thrust among rows 2 through 10 was within 30% for all scenarios. In Bathymetry B1 the spread is over 50% for 7D longitudinal spacing and over 100% for 11D between some rows. Each row of an array will experience a wide variation in thrust loads when sited over a bed that slopes in the flow direction.

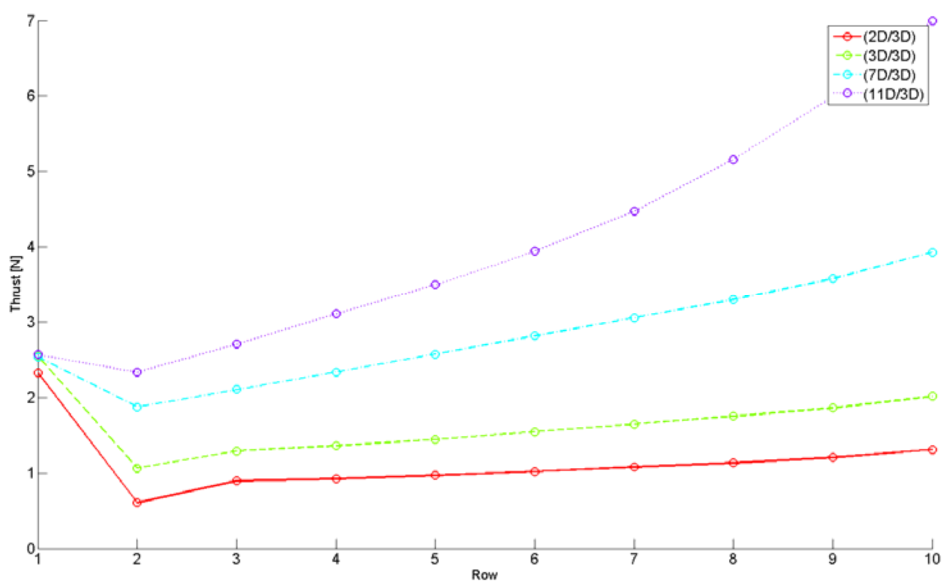

Figure 7.10: Thrust loads by rows for Bathymetry B1

While it is entirely expected that a bathymetry that promotes increasing velocities would likely result in increased loads within an array, a non-dimensionalization should provide a more comparative result. However, due to the increasing velocity the coefficient of thrust has to be formulated differently than for Bathymetries 0 and A. Equation 3.5 can be used to relate thrust loads to a coefficient of thrust. The problem lies with the definition of upstream velocity. In the reference bathymetry the upstream velocity was considered to be $0.25ms^{-1}$. If this velocity is used for each disk within the array in Bathymetry B1, then the coefficient of thrust could significantly exceed a value of 1 and would imply more energy was removed from the flow than was available. Consider the domain for Bathymetry B1, empty without an array. The inlet velocity is $0.25ms^{-1}$; however the flow over the bed is not because of continuity. The new flow velocity can be determined at any point over the bed by using equation 7.2. A better approximation for coefficient of thrust may be achieved by using the new flow velocities in equation 3.5. Instead of using the $0.25ms^{-1}$ for each row of disks, the new ideal, i.e. unobstructed, velocity at each row location from continuity can be applied. With the adjusted velocities the row and array coefficients of thrust become agnostic to the bathymetry. Figure 7.11 shows the curves for coefficients of thrust and power for the arrays of Bathymetry B1. Increasing the longitudinal spacing greater than 7D reaches a point where the coefficient of thrust is larger than one. Mathematically this forms a problem when solving Equation 3.5 because the corresponding axial induction factor, *a,* results a negative under the radical. At this point the coefficient of power decreases. This is a limit of the actuator disk model. In the actuator disk model increasing the axial induction factor past the Betz limit of 1/3 only increases the thrust loads not the power generation. In these simulations the thrust loads have increased to the point where the thrust loads continue to rise, but the power remains the same. The porous disks used in the simulation are not sized correctly or have the wrong porosity values to capture an optimal amount of energy from the flow. This is equivalent to choosing the wrong CEC for the flow. If devices were to be deployed in this flow field, they would need to be redesigned to capture an optimal amount of energy.

Figure 7.12 shows the coefficients of thrust and power for the array of 3D lateral spacing for Bathymetry 0 and B1. The arrays in Bathymetry B1 definitely have larger coefficients of thrust; however, the coefficient of power is not so clear. Every array with longitudinal spacing less than 7D has a higher coefficient of power in Bathymetry B1 than in the reference channel. At 7D longitudinal spacing the array coefficient of power was around the same as in the reference channel. The (11D/3D) array performed better in the reference channel than over the longitudinally sloping bottom. This is due the selection of porous disk in the array. If the disk was less porous or was sized larger, more energy could potentially be removed from the flow. For the selected porous disks, an array of (11D/3D) was not optimal for this bathymetry. The porous disks represent axial-flow turbines which means that different turbines would be required in the (11D/3D) array for optimal power generation. The bathymetry of this system completely changed the optimality of the array.

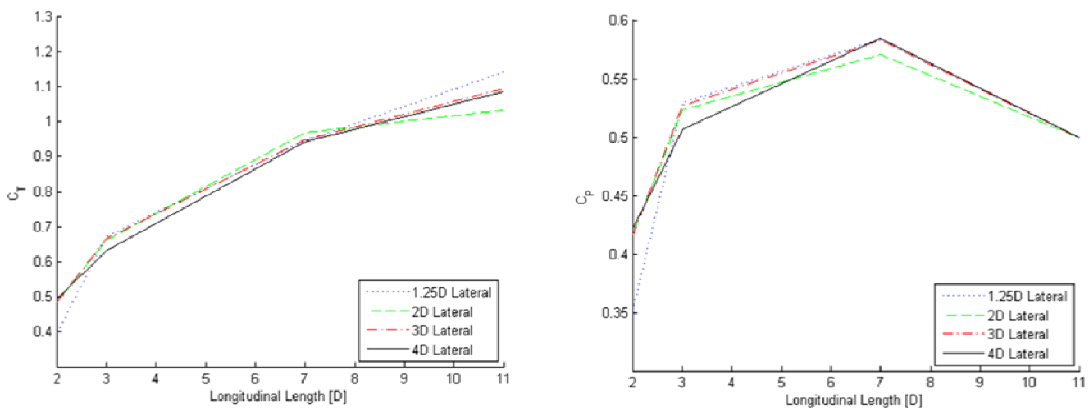

(a) (b)

Figure 7.11: Coefficients of thrust and power for Bathymetry B1, (a) coefficient of thrust, (b) coefficient of power

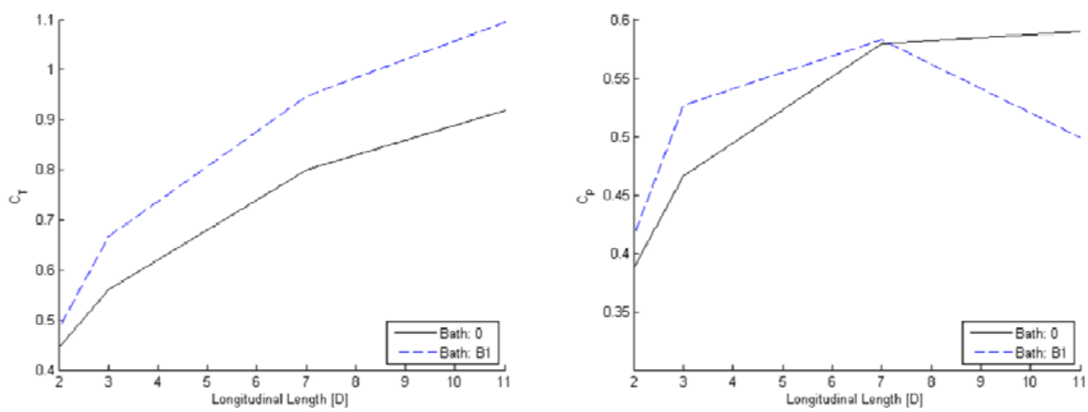

(a) (b)

Figure 7.12: Coefficient comparisons of Bathymetries 0 and B1 for 3D lateral spacing (a) coefficient of thrust, (b) coefficient of power

The wake recovery of Bathymetry B1 was different from Bathymetry 0. The wake recovery was recorded in terms of velocity deficit and evaluated from the last row of the array to the end of the domain. Figure 7.13 (a) shows the wake recovery for each array organized by longitudinal spacing and Figure 7.13 (b) shows the wake recovery for each array organized by lateral spacing. The wake recovery does not appear to have any correlation for recovery dependent on the lateral spacing. However, there is variation in the recovery profile dependent on longitudinal spacing. This is due to the placement of the arrays over the sloping bed. In Figure 7.13 there is were distinct minimums in the velocity deficit curves. The minimum occurs at the apex of the sloping bottom. Bathymetry B1 is referenced so that the first row of the array is located over the start of the sloped bed. The distance from the last row to the end of the sloped bottom changes for each longitudinal spacing. The wake profile is no longer the same across all the arrays due to the flow continuing to accelerate past the last row for all of the arrays with longitudinal distance less than 11D. Each array recovered to approximately the same velocity, but unlike Bathymetry 0 the wake recovery curves are not the same.

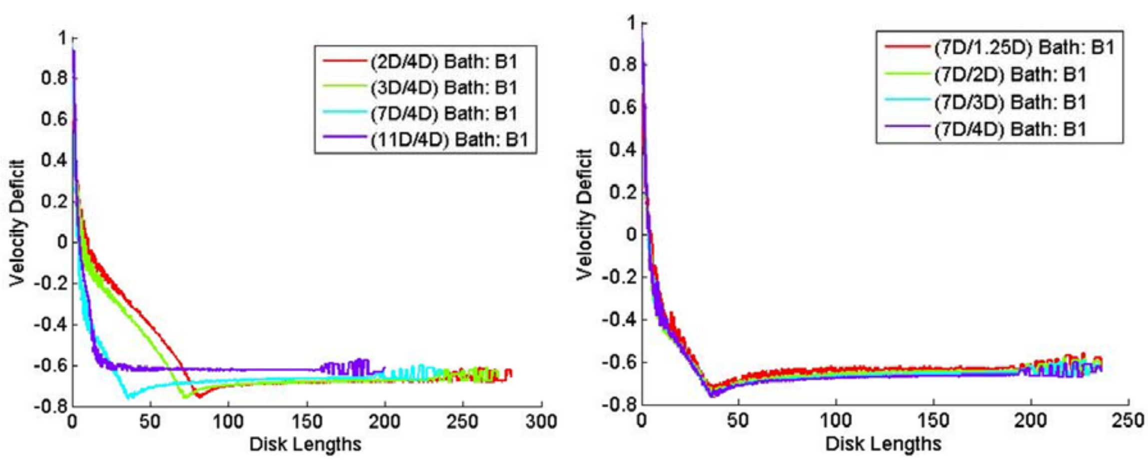

(a) (b)

Figure 7.13: Wake recovery for Bathymetry B1, (a) longitudinal spacing, (b) lateral spacing

Bathymetry B2

Bathymetry B2 is the same bathymetry as B1 except for the position of the arrays. In this bathymetry the arrays are referenced with their last row at the apex of the sloped bed. In Bathymetry B1 there were two effects that greatly increased thrust loads: velocity recovery between disks based on distance, as seen in Bathymetry 0, and the flow acceleration caused by mass conservation.

A new pattern emerged for Bathymetry B2 regarding the longitudinal spacing between the disks. The thrust loads increased as the longitudinal spacing increased, up until 7D at which point the thrust loads began to decrease. Figure 7.14 plots the array thrust curves for Bathymetry B1 versus the reference bathymetry. The changes in longitudinal spacing are greater than the reference scenario, but smaller than what was recorded in Bathymetry B1. The thrust loads in Bathymetry B2 start higher than its B1 counterparts; however, at 11D longitudinal length the thrust loads are the same because the 11D arrays of both bathymetry cases span the entire length of the sloping bed. Bathymetry B2 experiences higher thrust loads, relative to B1, at the shortest longitudinal spacing because those arrays begin further up the slope, so the velocity of the water has already increased due to continuity by the time the flow reaches the first rows.

The lateral spacing is inconsistent for performance in Bathymetry B2. Similarly to Bathymetry B1, the 1.25D lateral spaced arrays are relatively close in performance to the arrays with 2D, 3D, and 4D lateral spacing. The thrust is even larger than all other lateral spacings for 11D longitudinal spacing. This could be a unique result of both the mass conservation increasing flow velocities and the large velocity deficit behind each row causing a faster re-energization of the flow. This, coupled with a device fence not permitting pressure release between the devices, has the potential to have both increased velocity and the pressure differential across the actuator disks.

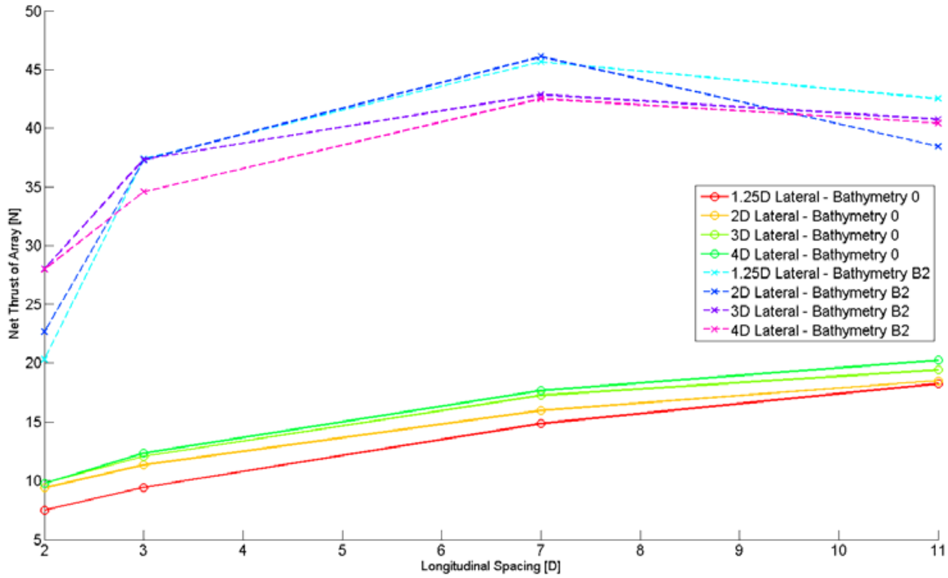

Figure 7.14: Total thrust loads for Bathymetries 0 and B2

The velocity profiles through the rows of the arrays in Bathymetry B2 are very similar to those of Bathymetry B1 with longitudinal spacing over 7D. None of the arrays converge to a set velocity deficit as was seen in the reference bathymetry. The increased flow speed from mass conservation dominated the velocity profile. Figure 7.15 shows the velocity deficit through the centerline of the array from the first row to the end of the domain. The velocity deficit decreased after each proceeding row in the array. Like in Bathymetry B1, the arrays with greater longitudinal spacing than 7D were able to reach a negative velocity deficit; which means that the flow speed increased past the inflow velocity.

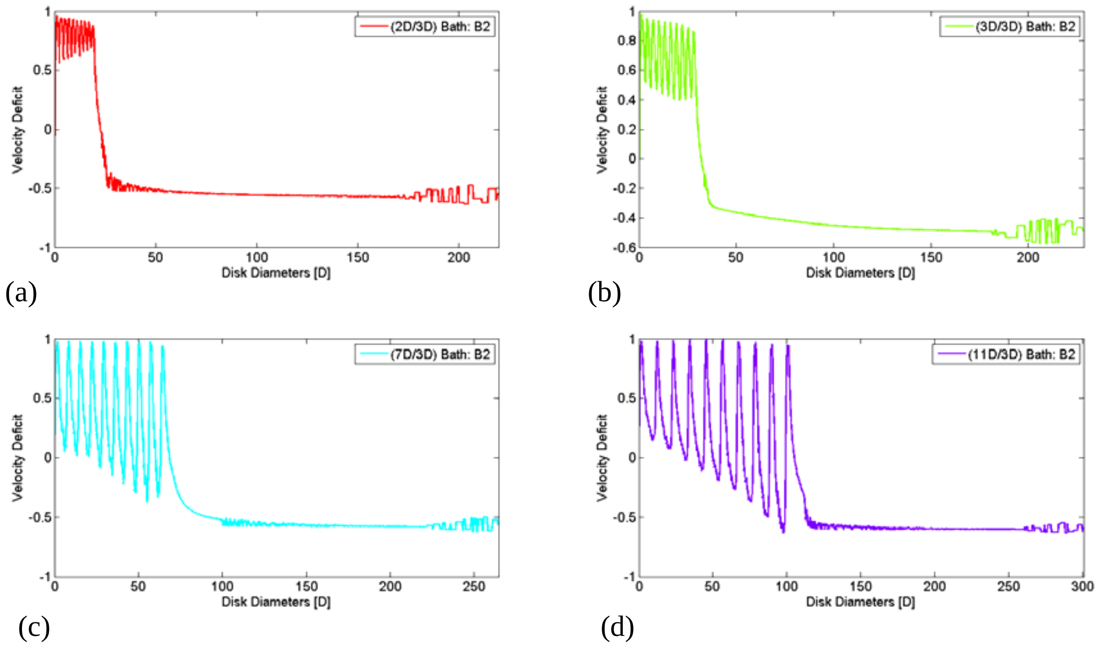

Figure 7.15: Velocity profiles by longitudinal spacing for Bathymetry B2 (a) (2D/3D), (b) (3D/3D), (c) (7D/3D), (d) (11D/3D)

Like with the other cases the velocity deficit curves are directly related to the thrust loads on the disks. The thrust loads on the rows of the arrays of Bathymetry B2 can be seen in Figure 7.16. The arrays with 2D and 3D longitudinal spacing have similar thrust loads to the reference bathymetry study. The first row experiences the largest loads and the last three row experience higher loads than the middle rows. The magnitude of the loads are just much larger. As in Bathymetry B1, the pattern breaks down at 7D and 11D longitudinal spacing. These arrays experience the loading condition where the last three rows experience the highest thrust. This is primarily due to the continuity effect. The spread in magnitude of thrust loads over the rows in the 7D and 11D longitudinally spaced arrays is similar to that found in Bathymetry B1. The overall thrust loads may be higher with 7D and 11D spacing, but the thrust loads can vary row to row by over 50%.

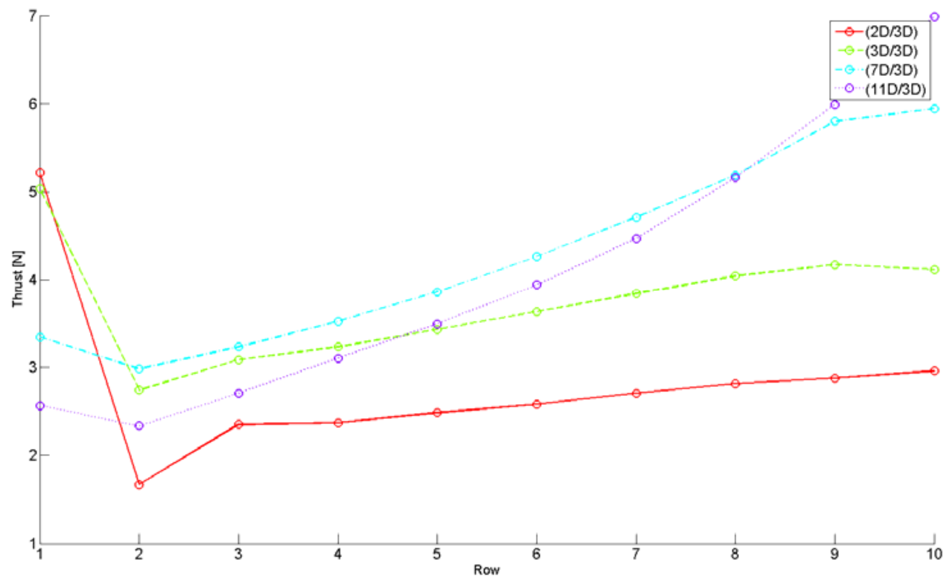

Figure 7.16: Thrust loads by row for Bathymetry B2

The coefficient of thrust curve for Bathymetry B2 follows the shape of the total thrust curves of the arrays, as seen in Figure 7.17. The coefficient of thrust substantially increased with each longitudinal spacing until 7D. After 7D spacing the coefficient of thrust slightly decreased for all the arrays. The two properties effecting the thrust loads are the longitudinal spacing and the conservation of mass over a decreasing area. The conservation of mass dominates the longitudinal spacing for thrust loads on the disks for longitudinal spacing over 7D. This does not occur in Bathymetry 0 and is unique for Bathymetry B2. Figure 7.18 shows the comparison between coefficient of thrust and power for Bathymetry 0 and B2 using the 3D lateral spaced arrays. The overall coefficient of thrust is higher for the arrays in bathymetry B2 than in Bathymetry 0. Additionally, the coefficient of power curves of Bathymetry B2 are substantially different when compared to expectations, i.e. Bathymetry 0, and even B1. In Bathymetry B2 the

3D longitudinal spacing produces nearly the same coefficient of power as it does with a 7D spacing and more than with a 11D distance between rows. The 7D and 11D arrays in Bathymetry 0 outperform those of Bathymetry B2 when the velocity increase is accounted for. In Bathymetry B2 the most optimal array would have a longitudinal spacing between 3D and 7D; at which point the maximum amount of power is captured without subjecting the devices to unnecessarily high thrust loads.

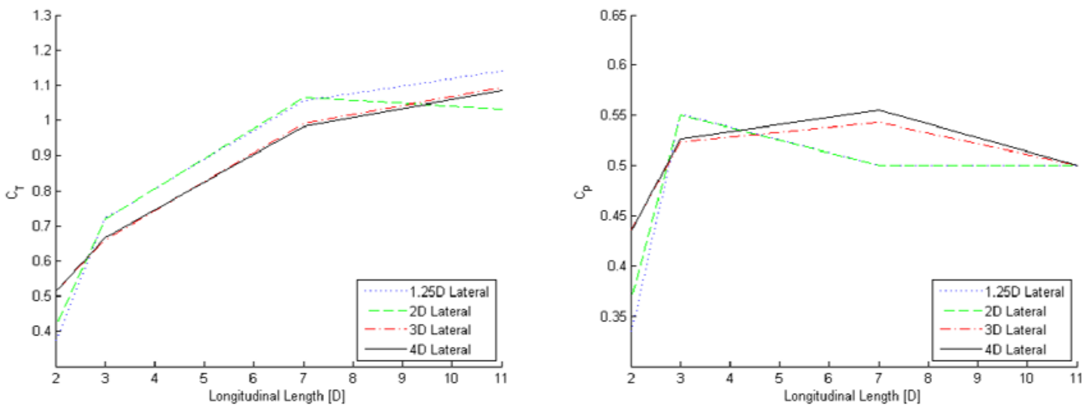

(a) (b)

Figure 7.17: Coefficients of thrust and power for Bathymetry B2, (a) coefficient of thrust, (b) coefficient of power

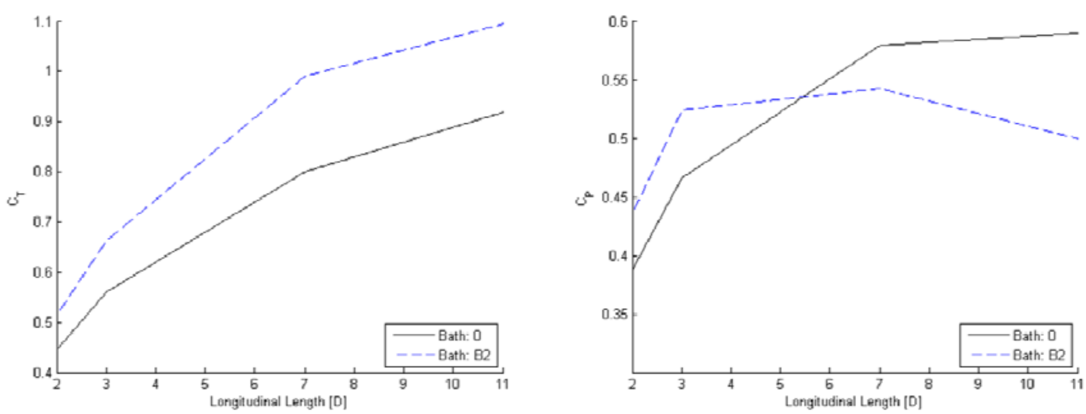

(a) (b)

Figure 7.18: Coefficient comparisons of Bathymetries 0 and B2 for 3D lateral spacing (a) coefficient of thrust, (b) coefficient of power

The wake recovery of Bathymetry B2 was more similar to the reference bathymetry than to Bathymetry B1. The wake recovery was in terms of velocity deficit and was evaluated from the last row of an array to the end of the domain in terms of device diameters. Figure 7.19 (a) shows the wake recovery for each array organized by 3D lateral spacing and Figure 7.19 (b) shows the wake recovery for each array organized by 11D longitudinal spacing. The wake recovery did not appear to have any correlation for recovery dependent on the longitudinal spacing. However, the 1.25D spaced arrays recovered slower than the rest of the lateral spaced arrays. The other lateral spaced arrays wakes recovery profiles followed the same curve. All of the wakes of Bathymetry B2 converged to a constant velocity deficit much faster than the other cases. In Bathymetry B2 all of the arrays are referenced to the end of the sloped bed. The flow velocity increases up until the end of the array due to conservation of mass, and the faster recovery is due to the flow reaching a maximum velocity at the end of the array.

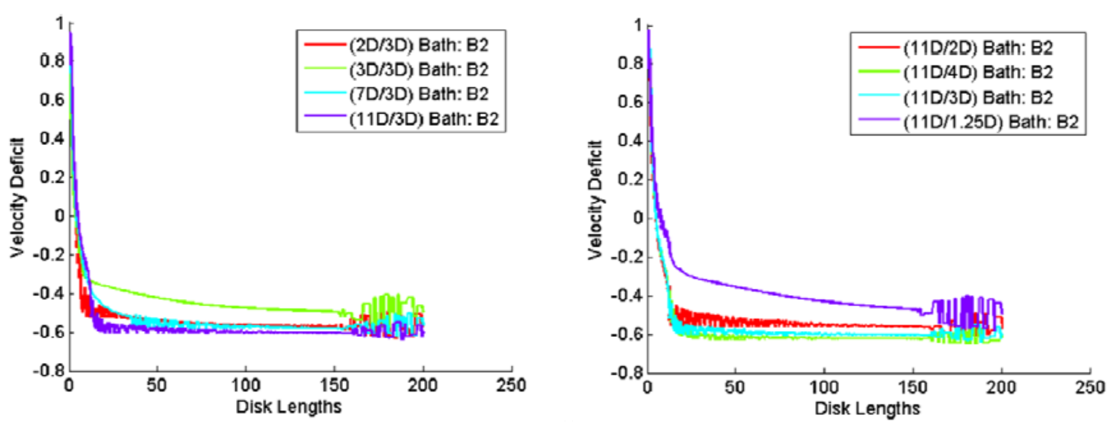

(a) (b)

Figure 7.19: Wake recovery for Bathymetry B2, (a) based on lateral spacing, (b) based on longitudinal spacing

Figure 7.20 shows the relationships between the coefficients of thrust and power between all the bathymetries for arrays with 3D lateral spacing. The 3D was chosen as a reference lateral spacing due to it optimality for most cases. Bathymetries 0 and A had near identical curves for coefficient of power and thrust. It is probable that developers could use a reference layout to determine optimal layouts in Bathymetry A. The coefficient thrust curves for Bathymetry B followed a similar profile as the others, but were substantially greater in magnitude. The coefficient of power curves for Bathymetry B did not follow the profile of the open channel reference as seen in Figure 7.20 (b). Due to the change in the profile for coefficient of power it would be impractical to design a layout for Bathymetry B using the reference channel.

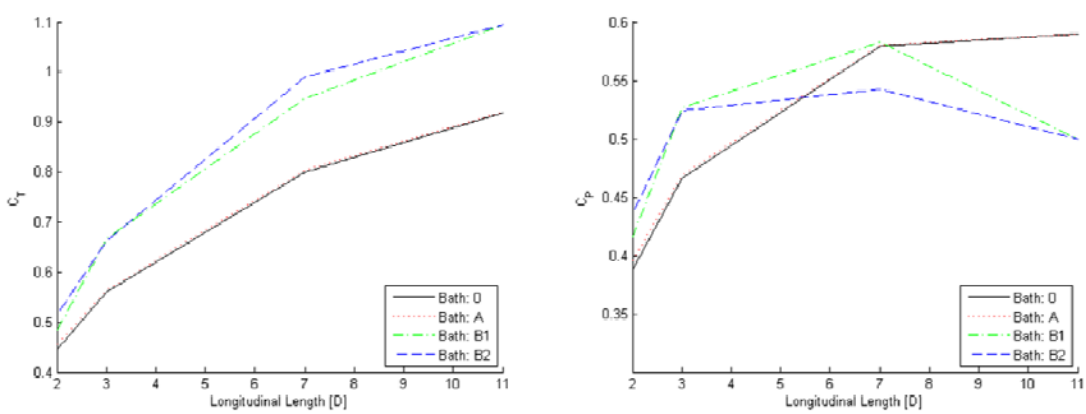

(a) (b)

Figure 7.20: Coefficient comparisons across all bathymetries for 3D lateral spacing, (a) coefficient of thrust, (b) coefficient of power

<u>Effect of Bathymetry</u>

Twenty array configurations were simulated over two bottom bathymetries. The thrust loads on the disks, velocity profiles through the center of the arrays, and wake recovery profiles were compared to an open channel reference study. Actuator disk theory was used to relate those thrust loads to a coefficient of thrust and power. At first it appeared that the bottom bathymetry would not have a substantial influence in array characteristics, as Bathymetry A had very similar trends in thrust loads and velocity profiles as the reference bathymetry. However, both scenarios for Bathymetry B provided substantially different results. The bottom topography in Bathymetry B caused the flow to accelerate through the array; which in turn increased thrust loads on the disks. In some cases the thrust loads were increased so much that the axial induction factor exceeded 1/3. Once this limit is met the thrust loads on the devices will increase, but no additional power generation will occur. Arrays that were optimized for Bathymetry 0 no longer performed in the same manner as in Bathymetry B. This proved that the bathymetry of a system can greatly affect characteristics of an array of devices.

The results of this bathymetric test study indicate that the site bathymetry must be considered when determining array performance. Bathymetry B demonstrated that substantial performance gains could be had based off of site bathymetry. As an example, appropriate placement of an array over a sloping bottom, similar to Bathymetry B, could be appropriately leveraged to increase the flow velocity through the array. Recall that thrust is based off the square of the velocity and power is based off the cube of the flow velocity. However, not all increased thrust loads are good for performance. While subtle differences in the bathymetry of a deployment site may not significantly affect array performance and optimization trends, Bathymetry B also proved that non-trivial optimizations of performance and loading may be missed if the additional flow effects due to changing domain shape are not taken into account.

Current-energy-converters need to be attached to generators in order to convert the kinetic energy of the flow to electrical energy that can be supplied to the grid. Each device has an optimum operating range. In Bathymetry 0 and Bathymetry A, the highest variance in thrust loads between rows 2 through 10 was within 30%. From a CEC deployment standpoint, it is desirable for each device to operate at similar conditions. With a small variance in loading between rows the same CEC could be deployed within the array. Once the variance becomes substantial, different CECs need to be considered for different sections of the array for optimal performance. In Bathymetry B1 the spread in thrust load over the rows of the (7D/3D) array was over 50%, which could mean potential for more performance. However, this performance gain could also prove to be a potential development problem as the large variance in thrust load between each row means at least some CECs will operating outside the optimal range; at which point device performance drops drastically. This may require installation of different turbines dependent upon their location in the array or turbines designed and optimized to operate in a much wider range of velocities. Though this latter option may produce a turbine that has a coefficient of power that is substantially less optimal over its range of operation than a single turbine designed for a particular velocity. It should be noted that that flow velocities change seasonally in most every deployment location. Even if CECs are specially selected for each row the variance in flow velocity over the year also has the potential to be detrimental to performance.

There presently is no standard convention for array comparisons. This thesis adapted the actuator disk model to be applied to arrays, so that each array had its own axial induction factor, coefficient of thrust, and coefficient of power. The actuator disk model is dependent on an upstream velocity value for a device which can be used in conjunction with thrust to obtain an axial induction factor. The definition of upstream velocity becomes problematic when discussing an array. The standard convention is to use the initial upstream velocity for each row of devices; however, the addition of bathymetry puts this convention to question. In the case of Bathymetry B the flow area decreases over length, so the velocity increases inside the domain due to conservation of mass. This thesis proposes that the continuity equation should be used to adjust the inlet flow velocity for the change in location over a sloped bottom. This adjustment to the upstream velocity in the actuator disk model could normalize the flow for any bathymetry. Once the bathymetric velocities have been non-dimensionalized, it can be compared to any other array model. This was done for Bathymetry B to compare with Bathymetries 0 and A. The coefficients of thrust and power then can be used to determine array performance.

CONCLUSION

The research conducted in this thesis was done to determine if site bathymetry needs to be taken into account when deploying arrays of MHK devices. Every potential deployment location whether off the coast or in a river will have a unique bathymetry. Up to this point research into array development has mostly been based off of wind farms where most topological effects are ignored or are negligible. And the research into marine hydrokinetics has been primarily single device performance and small arrays in open channels. The research presented here found that studies done for array performance in flat bottom or open channels are not guaranteed to correlate well to real world locations. The study used computational fluid dynamics to model arrays of current energy converters over two bottom bathymetries. Porous disks were used to simulate CECs, and more specifically horizontal-axis-water-turbines. The CFD physical parameters were calibrated against an experiment performed by researchers at the University of Southampton. The model was then expanded to fit an array of porous disks in an open channel. Twenty arrays were tested in the open channel to establish a baseline set of data for uninterrupted array performance. The arrays were then placed over two different bathymetries and new performance data was collected. The data collected showed that the bathymetry of a site has the potential to completely change the performance characteristics on an array and the definition of an optimized array.

Bathymetry 0 was created to formulate a baseline set of data for array characteristics in an open channel. Twenty arrays were tested over the open channel to establish a baseline of performance curves using thrust loads and array spacing, as well as wake recovery profiles. For each array layout, it was found that the longitudinal spacing had a more significant impact on performance than the lateral. As the longitudinal spacing increased the more distance the flow had to recover behind a device. After enough space between individual devices the flow reached a maximum recovery where any additional increase in length would no longer effect flow recovery. Performance gains were present with increased lateral spacing, but they were substantially smaller. The optimal performance for lateral spacing was reached by spacing the devices far enough laterally so the flow was able to fully develop around each individual device within the array. The wake recovery profiles for each array were very similar and converged to the same downstream wake profile.

Bathymetry A introduced a sloping bottom across the width of the channel. This geometry was similar to that found in some close-to-shore locations. Sixteen arrays were tested to determine thrust load curves and wake recovery profiles for the new bathymetry. Bathymetry A had slightly higher loading on the disks than Bathymetry 0, but the performance curves based on thrust loads and device spacing followed the same trends. The results suggest that an open channel array could be used to model a lateral sloping bathymetry. However, the other bathymetry study proved this does not translate to all domains.

Bathymetry B introduced a sloping bottom in the flow direction. This topography could be related to certain sections of river undergoing a noticeable vertical height change or within a tidal strait. Two different deployment locations were tested for thrust loads and wake recovery profiles. The first deployment location, B1, referenced the arrays from the first row to the start of the sloped bathymetry, and the second, B2, referenced the arrays from the last row to the apex of the sloped bed. The thrust loads in B1 increased as the longitudinal spacing between rows increased. The change in thrust loads between each array were much larger than in Bathymetry 0 or A. This was attributed to conservation of mass for an incompressible fluid. The cross-sectional area of the domain decreased over the length of the sloped bottom, which caused the flow velocity to increase. The wake recovery profiles of Bathymetry B1 were found to be dependent on longitudinal spacing; which was not observed for any other bathymetry. Bathymetry B2 had the same trend that was found for thrust loads as Bathymetry B1 up to seven device diameter longitudinal spacing; at which point the thrust loads decreased. Each array experienced higher inflow velocities due to the rear location over the sloped bottom. The increase in velocity was enough to raise the coefficient of thrust over 0.9. A coefficient of thrust of 0.9 correlates to the Betz limit and any additional thrust does not increase power generation. Bathymetry B2 had the quickest wake recovery profiles; which was caused by the rearward location of the arrays. The flow finished accelerating at the last row of the arrays due to conservation of mass.

The bathymetry of a deployment location has the potential to drastically change array performance properties, as was shown with both cases of Bathymetry B. The main source of absolute performance change was due to continuity. It may be possible for array developers to take advantage of the site bathymetry to increase array performance. Bathymetry B proved that there was more potential for absolute power production by placing arrays over a positively sloping bed in the flow direction. This may not hold true for negatively sloping bed as the velocity decrease from continuity will be coupled with the natural wake behind each device. A deployment problem is introduced on how to address the varied loading within an array for each individual row. Some rows in the arrays experienced relative loads that were over 50% different than other rows in the same array. Water turbines are designed to operate efficiently at particular flow velocities. If the flow velocities vary substantially from row to row, only a couple of rows would be operating efficiently. To take advantage of the location bathymetry it may require that each turbine is designed based on the row which it will be deployed.

Regardless, array configurations optimized within an open channel will not demonstrate the same trends or performance when moved to more complex locations. In Bathymetry 0 the arrays with the highest longitudinal spacing performed the best; whereas in Bathymetry B the arrays with substantially smaller spacing performed similarly. The bathymetry forced the velocity to increase through the arrays, thus increasing the coefficient of thrust for the arrays. An increase in coefficient of thrust over 0.9 results in higher thrust loads, but no change in power generation for the array. In order to design the arrays to optimally operate the bathymetry must be accounted for.

Coefficients of thrust and power for an array need to use the undisturbed velocities that are local to each device. Deployment locations potentially have velocity fields that are created by the local bathymetry. Unlike an individual device, which only experiences an undisturbed inflow velocity, an array of devices will have multiple devices operating within the wake of other, more upstream devices. To gain an accurate coefficient of thrust and power for the array as a whole, each device within the array will need to utilize its individual coefficient of thrust and power based on its local velocity. Once these local device velocities have been adjusted, an array coefficient of thrust and power can be calculated and compared the array used in two completely different bathymetries.

The research presented in this thesis could be expanded in a number of ways. To further verify the RANS model, LES simulations could be performed over each bathymetry using one of the arrays to compare thrust and wake recovery data. It would also be useful to create experiments using arrays porous disks over sloped bottoms in a flume to compare to the numerical results presented in this paper. Array performance based on distance to the channel bed could also be explored to determine the height that CECs need to be deployed to negate bathymetric effects. The simulations done in this thesis limited the devices to a plane at a specific depth. Arrays can also be created so that the internal devices operate at various depths. This could be a much more efficient way to design arrays as the first row of devices at each depth experience uninterrupted flow.

REFERENCES CITED

Allmaras, S., Johnson, F., Spalart, P. "Modifications and Clarifications for the Implementation of the Spalary-Allmaras Turbulence Model." Seventh International Conference on Computational Fluid Dynamics (ICCFD7). Hawaii (July 2012)

Aloui, F., M. Kardous, R. Cheker, S. Ben Nasrallah. "Study of the wake induced by a porous disk." 21st Congress Fracais de Mecanique (2013)

Anderson, R., Morrison, M., Sinclair, K., Strickland, D., Davis, H., and Kendall, W. “Studying Wind Energy/Bird Interactions: A Guidance Document.” Avian Subcommittee & National Wind Coordinating Committee (December 1999)

Archer, Cristina L., Sina Mirzaeisefat, and Sang Lee. "Quantifying the sensitivity of wind farm performance to array layout options using large-eddy simulation." Geophysical Research Letters, Vol. 40, 4963-4970 (2013)

AWEA, "Anatomy of a Wind Turbine." American Wind Energy Association. (2013). Accessed April 1, 2015. http://www.awea.org/Resources/Content.aspx?ItemNumber=5083

Bang, D., Polinder, H., Ferreira, J., Rooij, R. "New Active Speed Stall Control compared to Pitch Control for a Direct-Drive Wind Turbine." EWEC (2007)

Batten, W. M. J., Harrison, M. E., Bahaj, A. S. “Accuracy of the actuator disc-RANS approach for predicting the performance and wake of tidal turbines.” Phil. Trans. R. Soc. 2013 371, 20120293, published online (January 2013)

Blackmore, T., Batten, J., Bahaj, A. S., “Influence of turbulence on the wake of a marine current turbine simulator.” The Royal Society Publishing, DOI: 10.1098/rsp.2014.0331 (August 2014)

Bunn, M., Yokochi, A., "Testing and Accelerated Aging of Conductive Antifouling Paints for Marine Applications." GMREC, Marine Energy Technology Symposium, Seattle, WA. (April 2014)

Burton, Jenkins, Sharpe, and Bossanyi, Wind Energy Handbook 2 Edition. Wiley (2011) 39-43

Cada, G., Copping, A., Roberts, J. "Identifying How Marine and Hydrokinetic Devices Affect Aquatic Environments" Hydro Review (April):22-27

Cameron, M. "Flow Field Measurements for a Cross Flow Turbine." Thesis. University of Maine (August 2012)

Churchfield, M. J., Lee, S., Moriarty, P. J., Martinez, L. A., Leonardi, S., Vijayakumar, G., and Brasseur, J. G. “A Large-Eddy Simulation of Wind-Plant Aerodynamics,” 50th AIAA Aerospace Sciences Meeting (January 2012)

Cleynen, O., "Wing proile nomenclature." Wikimedia Commons. Accessed May 14, 2015. http://commons.wikimedia.org/wiki/File:Airfoil.svg (April 2011)

Crasto, G. and Gravdahl, A. R. "CFD wake modeling using a porous disc." European Wind Energy Association. (2008)

Daly, T., Myers, L., Bahaj, S. "Modelling of the flow field surrounding tidal turbine arrays for varying positions in a channel." Royal Society Publishing (January 2013)

Drew, B., Plummer, A., Sahinkaya, M., "A review of wave energy converter technology." Proceedings of the Institution of Mechanical Engineers, Part A: Journal of Power and Energy, Vol. 223, No. 8, pp. 887-902.

Dubbs, L., Keeler, A., O'Meara, T. "Permitting, RIsk and Marine Hydrokinetic Energy Development." The Electricity Journal (2013)

EPRI, “Assessment and Mapping of the Riverine Hydrokinetic Energy Resource in the Continental United States.” EPRI, Palo Alto, CA (2012) 1026880.

EPRI, "Mapping and Assessment of the United States Ocean Wave Energy Resource." EPRI, Palo Alto, CA: 2011 1024637

EMEC, "Wave Devices." European Marine Energy Centre LTD (2015). Accessed April 1, 2015. http://www.emec.org.uk/marine-energy/wave-devices/

Ferreira, Carlos Simao. "The Near Wake of the VAWT 2D and 3D Views of the VAWT Aerodynamics." Thesis. Delft University of Technology (October 2009)

GE, "Battery Technology for Wind Energy Storage | GE Renewable Energy." Battery Technology for Wind Energy Storage | GE Renewable Energy. Accessed May 15, 2015. (2015) https://renewables.gepower.com/wind-energy/technology/integrated-storage.html

Harrison, M. E., Batten, L. E. Myers, and A. S. Bahaj. "A comparison between CFD simulations and experiments for predicting the far wake of horizontal axis tidal turbines." 8th European Wave and Tidal Energy Conference (2009)

Haas, K., Yang, X., Fritz, H. "Modeling Impacts on Energy Extraction from the Gulf Stream System." GMREC, Marine Energy Technology Symposium, Seattle, WA. (April 2014)

Haas, K., Fritz, H. M., French, S. P., Neary, V. “Assessment of Energy Production Potential from Ocean Currents along the United States Coastline” Georgia Tech Research Corporation. Award Number DE-EE0002661 (2013)

Haas, K., Fritz, H. M., French, S. P., Smith, B. T., Neary, V. “Assessment of Energy Production Potential from Tidal Streams in the United States” Georgia Tech Research Corporation. Award Number DE-FG-08GO18174 (2011)

James, S. C., Lefantzi, S., Barco, J., Johnson, E., and Roberts, J. D. “Verifying Marine-Hydro-Kinetic Energy Generation Simulations Using SNL-EFDC,” Oceans 2011, (September 2011)

Johnson, E., Barco J., James, S., and Roberts, J. "Reference Model MHK Turbine Array Optimization Study within a Generic River System." Sandia Report SAND2011-9305 (November 2011)

Johnson, M., Fahnline, J., Johnson, E., Barone, M., Fontaine, A. "Influence of Blade Solidity on Marine Hydrokinetic Turbines." Proceeding of the Internoise/ ASME NCAD meeting (August 2012)

Jones, C., Magalen, J., Roberts, J. "Wave Energy Converter (WEC) Array Effects on Wave, Current, and Sediment Circulation: Monterey Bat, CA." Sandia Report, SAND2015-17401 (September 2014)

Kang, S., Borazjani, I., Colby, J., Sotiropoulus, F. "Numerical simulation of 3D flow past a real-life marine hydrokinetic turbine." Advances in Water Resources (January 2012)

Lehman, K. "Montana’s ‘Windustry’ Poised to Grow." New West. (March 2008). Accessed April 1, 2015. http://newwest.net/topic/article/montana_windustry_poised_for_growth/C38/L38/

Lignarolo, L.E.M., Ragni, D., Ferreira, C.J., van Bussel, G.J.W., “Turbulent mixing in wind turbine and actuator disk wakes: an experimental analysis.” AIAA SciTech, 33rd Wind Energy Symposium. (January 2015)

Maalouf, B., Massouh, F., Dobrev, I., "Vortex structure in the wake of a wind turbine rotor." 19ème Congrès Français de Mécanique (2009)

Malki, R., Masters, I. “Planning tidal stream turbine array layouts using a couple blade element momentum – computational fluid dynamics model.” Renewable Energy, (March 2014), 46-54

Miller, D., Mandell, J., Samborsky, D., Hernandez-Sanchez, B., Griffith, D. "Performance of Composite Materials Subjected to Salt Water Environments" AIAA Wind Energy Session (2012)

Morgan J., “The Catch-22 of Energy Storage.” Chemistry in Australia, (August 2014) pp 22-24

Mozafari, Amir Teymour Javaherchi. “Numerical investigation of Marine Hydrokinetic Turbines: methodology, and applications to flume and full-scale reference models.” Dissertation University of Washington (2014)

Mujadi, E., Butterfield, C. "Pitch-Controlled Variable-Speed Wind Turbine Generation" IEEE Industry Applications (1999)

Mulvany, N., Chen, L., Tu, J., Anderson, B. "Steady-State Evaluation of 'Two-Equation' RANS (Reynolds-averaged Navier Stokes) Turbulence Models for High-Reynolds Number Hydrodynamic Flow Simulations." Australian Government, Department of Defense, Defense Science and Technology Organization. (2004)

Murray, J.C. and Barone, M., (2011). “The Development of CACTUS, a Wind and Marine Turbine Performance Simulation Code,” 49th AIAA Aerospace Sciences Meeting (January 2011)

Myers, L. E., Bahaj, A. S. “An experimental investigation simulating flow effects in first generation marine current energy converter arrays.” Renewable Energy Journal (July 2011)

NASA, "Turbulence Modeling Resource." NASA. Accessed April 1, 2015. http://turbmodels.larc.nasa.gov/.

Neary, V. S., Chamorro, L. P., Hill, C., Gunawan, B., and Sotiropoulos, F. “US Department of Energy National Lab Activities in Marine Hydrokinetics: Machine Performance Testing,” 4th International Conference on Ocean Energy, (October 2012)

Niblick, A. "Experimental and Analytical Study of Helical Cross-Flow Turbines for a Tidal Micropower Generation System." Thesis. University of Washington (2012)

O'Dea, A., Haller, M. "Analysis of the Impcats of Wave Energy Converter Arrays on the Nearshore Wave Climate." GMREC, Marine Energy Technology Symposium, Seattle, WA. (April 2014)

Patricio, S., Soares, C., Sarmento, A. "Underwater Noise Modeling of Wave Energy Devices." Eighth European Wave and Tidal Energy Conference (2009)

Roadman, J., Huskey, A., “Acoustic Noise Test Report for the SWIFT Wind Turbine in Boulder, CO.” National Renewable Energy Laboratory, NREL/TP-5000-58244 (April 2013)

Roberts, J., Johnson, E., James, S. "SNL-EFDC Model Application to Scotlandville Bend, Mississippi River." TETHYS (2012)

Roberts, J., Nelson, K., Jones, C., James, S. "A Framework for Optimizing the Placement of Current Energy Converters." Second Marine Energy Technology Symposium, Seattle, WA (April 2014)

Rogers, A., Manwell, J., Wright, S. “Wind Turbine Acoustic Noise.” Renewable Energy Research Laboratory, Department of Mechanical and Industrial Engineering, University of Massachusetts at Amherst. (2006)

Romero-Gomez, P., Richmond, M. "Discrete Element Modeling of Blade-Strike Frequency and Survival of Fish Passing Through Hydrokinetic Turbines." GMREC, Marine Energy Technology Symposium, Seattle, WA. (April 2014)

Sale, D., Aliseda, A., Li, Y. "Simulation of Hydrokinetic Turbines in Turbulent Flow using Vortex Particle Methods." Marine Energy Technology Symposium METS (April 2014)

Salter, S. "Are Nrealy all Tidal Stream Turbine Designs Wrong?" Fourth International Conference on Ocean Energy (October 2012)

Sherry, M., Sheridan, J., Jacono, D. "Characterization of a horizontal axis wind turbine's tip and root vortices." Exp Fluids (2013) 54:1417 DOI 10.1007/s00348-012-1417-y (2013)

Siemens, “Wind power solutions for onshore, offshore and service projects.” Accessed April, 1, 2015. http://www.energy.siemens.com/hq/en/renewable-energy/wind-power/ (2015)

Smith, R. "Symscape." Anatomy of a Horizontal-Axis Wind Turbine. (May 2007). Accessed April 1, 2015. http://www.symscape.com/blog/anatomy_horizontal_wind_turbine

SNL, "Offshore Ambitions for the Vertical-Axis Wind Turbine." Sandia National Laboratories (2012). Accessed April 1, 2015.

http://energy.sandia.gov/offshore-ambitions-for-the-vertical-axis-wind-turbine/

Spalart, P., Allmaras, S., "A One-Equation Turbulence Model for Aerodynamic Flows." Recherche Aerospatiale, No. 1, 1994, pp, 5-21.

Stevens, R., Gayme, D., Meneveau, C. "Large Eddy Simulations studies of the effects of alignment and wind farm length." Journal of Renewable and Sustainable Energy (May 2015)

Sun, X. "Numerical and Experimental Investigation of Tidal Current Energy Extraction." Thesis. University of Edinburgh (2008)

Tawade, S., Todkar, S., Hade, A. "Fatigue Life Optimization of Wind Turbine Blade." International Journal of Research in Engineering and Technology, Volume 3, Special Issue, 3. NCRIET (2014)

Thyng, K. M., Roc, T. "Tidal current turbine power capture and impact in an idealized channel simulation." European Wave and Tidal Conference (2013)

Tomichek, C., Coly, J., Andoizio, M., Frisk, M., Dunton, K., Fox, D., Jordaan, A. "Tagged Species Detection: Approach to Monitoring Marine Species at Marine Hydrokinetic Projects." GMREC, Marine Energy Technology Symposium, Seattle, WA. (April 2014)

Viehman, H., Zydlewski, G. "Fish Interactions with a Commercial-Scale Tidal Energy Device in the Natural Environment" Estuaries and Coasts. S241-S252, DOI 10.1007/s12237-014-9767-8 (2015)

Wan, Y., Bucaneg, D. Jr., "Short-Term Power Fluctuations of Large Wind Power Plants." Journal of Solar Energy Engineering: Transactions of the ASME; Vol. 124, NREL/CP-500-33842. Doi:10,1115/1.1507762, (November 2002), pp. 427-431

Wan, Yih-huei., "Analysis of Wind Power Ramping Behavior in ERCOT." NREL, NREL/TP-5500-49218 (March 2011)

Wan, Y., "Long-Term Wind Power Variability." NREL, NREL/TP-5500-53637 (January 2012)

Whittlesey, R.W., Liska, S. and Dabiri, J. O. "Fish schooling as a basis for vertical axis wind turbine farm design." IOP Publishing, Bioinsp, Biomim. (2010)

WPP,"17. The Betz Limit - and the Maximum Efficiency for Horizontal Axis Wind Turbines .Can It Be Exceeded and Does It Apply to Vertical Axis Wind Turbines?"

Windpower program Accessed April 1, 2015. http://www.wind-power-program.com/betz.htm

WRA, “Bridging the gap, Montana harness strong winds in the west.” Western Resource Advocates Accessed April 1, 2015. (2015) http://www.westernresourceadvocates.org/energy/CEP/CEPMT.pdf

Wu, Yu-Ting and Porté-Agel, F." Large-Eddy Simulation of Wind-Turbine Wakes: Evaluation of Turbine Parameterizations." Springer Science+Business Media (2010)

Yang, X., Kang, S., Sotiropoulos, F. "Toward A Simulation-Based Approach for Optimizing MHK Turbine in Natural Waterways." Marine Energy Technology Symposium METS (April 2013)

Yang, Z., Wang, T., Copping, A. "Array Optimization for Tidal Energy Extraction in a Tidal Channel - A Numerical Modeling Analysis." GMREC, Marine Energy Technology Symposium, Seattle, WA. (April 2014)

Xiao, H., R., Sui, R., Duan, L., and Rösgen, T. "Experimental Investigations of Turbulent Take Behind Porous Disks." Marine Energy Technology Symposium METS (April 2013)